Sensitivity of simulated flow fields and bathymetries in meandering channels to the choice of a morphodynamic model

Rousseau, Y. Y. , Biron, P. M. and Van De Wiel, M. J.

Original citation & hyperlink:
Rousseau, Y. Y. , Biron, P. M. and Van De Wiel, M. J. (2015) Sensitivity of simulated flow fields and bathymetries in meandering channels to the choice of a morphodynamic model. Earth Surface Processes and Landforms, volume (In Press)
http://dx.doi.org/10.1002/esp.3885

ISSN 0197-9337
ESSN 1096-9837
DOI 10.1002/esp.3885

Earth Surface Processes and Landforms

Sensitivity of simulated flow fields and bathymetries in meandering channels to the choice of a morphodynamic model

Journal:	*Earth Surface Processes and Landforms*
Manuscript ID	ESP-15-0052.R1
Wiley - Manuscript type:	Paper
Date Submitted by the Author:	n/a
Complete List of Authors:	Rousseau, Yannick; University of Western Ontario, Geography Biron, Pascale; Concordia University, Geography, Planning and Environment Van de Wiel, Marco; Coventry University, Centre for Agroecology, Water and Resilience (CAWR)
Keywords:	morphodynamic models, river channel morphology, meandering, sediment transport, computational fluid dynamics

Sensitivity of simulated flow fields and bathymetries in meandering channels to the choice of a morphodynamic model

Yannick Y. Rousseau[1], Pascale M. Biron[2], Marco J. Van de Wiel[3]

ABSTRACT: Morphodynamic models are used by river practitioners and scientists to simulate geomorphic change in natural and artificial river channels. It has long been recognized that these models are sensitive to the choice of parameter values, and proper calibration is now common practice. This paper investigates the less recognized impact of the choice of the model itself. All morphodynamic models purport to simulate the same flow and sediment dynamics, often relying on the same governing equations. Yet in solving these equations, the models have different underlying assumptions, for example regarding spatial discretization, turbulence, sediment inflow, lateral friction, and bed load transport. These differences are not always considered by the average model user, who might expect similar predictions from calibrated models. Here, a series of numerical simulations in meandering channels was undertaken to test whether six morphodynamic codes (BASEMENT, CCHE-2D, NAYS, SSIIM-1, TELEMAC-2D and TELEMAC-3D) would yield significantly different equilibrium bathymetries if subjected to identical, initial flow conditions. We found that, despite producing moderately similar velocity patterns on a fixed-flat bed (regression coefficient r of 0.77 ± 0.20), the codes disagree substantially with respect to simulated bathymetries (r = 0.49 ± 0.31). We relate these discrepancies to differences in the codes' assumptions. Results were configuration specific, i.e. codes that perform well for a given channel configuration do not necessarily perform well with higher or lower sinuosity configurations. Finally, limited correlation is found between accuracy and code complexity; the inclusion of algorithms that explicitly account for the effects of local bed slope and channel curvature effects on transport magnitude and direction does not guarantee accuracy. The range of solutions obtained from the evaluated codes emphasises the need for carefully considering the choice of code. We recommend the creation of a central repository providing universal validation cases and documentation of recognized fluvial codes in commonly studied fluvial settings.

KEYWORDS: morphodynamic models; river channel morphology; meandering; sediment transport; computational fluid dynamics.

---

[1]Yannick Y. Rousseau (yanrousseau@gmail.com); Ph.D. Candidate, Department of Geography, University of Western Ontario, 1151 Richmond Street, London, Ontario, Canada, N6A 5C2, +1 (519) 914-1316.

[2]Pascale M. Biron (pascale.biron@concordia.ca); Associate Professor, Department of Geography, Planning and Environment, 1455 de Maisonneuve Blvd W., Montréal, Québec, Canada, H3G 1M8, +1 (514) 848-2424 x2061.

[3]Marco Van De Wiel (marco.vandewiel@coventry.ac.uk); Reader, Centre for Agroecology, Water and Resilience (CAWR), Coventry University, Priory Street, Coventry, CV1 5FB, United Kingdom, +44 (0) 2477 651675.

Introduction

Morphodynamic models, i.e. computational hydraulics models coupled with a sediment transport module, are often employed to predict erosion and deposition zones in river channels, and to examine flow hydraulics, channel morphology, and interactions between a channel and established riparian communities (e.g. Bates et al., 2005; Rinaldi et al., 2008; Ham and Church, 2012; Mosselman, 2012). Accessibility to morphodynamic models has greatly improved since their introduction in the 1980s, with key aspects including: more detailed documentation; a broader community of users, combined with better communication platforms; low or no purchase cost; and the ability to run models on inexpensive, powerful, multiprocessing personal computers. These models are now commonly used for morphodynamic modelling in one-, two- and three-dimensions (1D, 2D and 3D) (Darby and Van de Wiel, 2003).

Despite the improved accessibility to computational fluid dynamics (CFD) and morphodynamic models, investigations are generally carried out using a single modelling code. Thus, the consequences of selecting any given modelling code on river channel predictions are largely ignored. In contrast, the level of uncertainty associated with model predictions is commonly dealt with in several other scientific disciplines involving stochastic phenomena, for example in ecological modelling (Jiao et al., 2008), hydrology (Franz et al., 2010) or climate modelling, by providing a set of climate predictions from an ensemble of different models (Bates et al., 2008; Gregow et al., 2011; Fischer et al., 2012). In river-related investigations, the appropriate code should be the one that best reproduces river channel dynamics in natural systems. Because there is no a priori knowledge of which code is most appropriate for a given environmental context, model comparison studies provide useful information on the range of possible outcomes.

Although guidelines exist for modellers to determine whether results from a simulation can be deemed reliable (Roache et al., 1986; Lane et al., 2005), some of the subtleties in the models' underlying assumptions may be lost on the average model user who, given that the models are based on the same governing equations, might expect that different models, when properly calibrated, will generate very similar predictions. However, differences in sub-models, algorithms, simplifications, and other modelling options may well result in various levels of accuracy for different configurations. For example, Rameshwaran et al. (2013) used a single channel layout (a meander with medium sinuosity of 1.37) in their comparative study, but would a consistent level of accuracy of each model have been observed for a lower or higher sinuosity channel? We argue that the value of inter-comparison studies lies in the opportunity they provide to identify the most relevant algorithms and solver options for any particular context, to determine the range of applicability of modelling codes to fluvial channel types, and to improve codes and procedures.

One of the difficulties in comparing different codes is to ensure that they are indeed comparable, i.e. that the governing equations, boundary and initial conditions, numerical mesh, etc. are identical. Since each code has its own specificities, for example on the available choice of turbulence models or sediment transport equations, bed roughness parameterisation, active layer management, etc., it is impossible to achieve perfectly identical model configurations in a comparative study. The suggested approach here is to use identical channel layout, initial flow and boundary conditions, and calibration procedure between codes.

The objectives of this study are 1) to evaluate whether different 2D and 3D morphodynamic modelling codes generate substantially divergent flow fields and equilibrium bathymetries for an identical set of imposed boundary conditions and nearly-identical set of options, sub-models and parameter values, and 2) to assess whether model performance varies with channel configuration. The accuracy of the numerical models is assessed by comparing predictions to measurements obtained in three analogue flume experiments with varying degrees of sinuosity.

Methodology

Numerical codes

Four 2D and two 3D morphodynamic codes are evaluated: BASEMENT v. 2.2.1021 (B_2), CCHE-2D v. 3.29.0 (C_2), NAYS v. 2.1.7.3285 (N_2), the 2D and 3D versions of TELEMAC v. 6.2 (T_2, T_3), and the 3D code SSIIM-1 v. 43 (S_3). These codes are thoroughly described in Fäh et al. (2011), Jia and Wang (2001a), Shimizu et al. (2013), Galland et al. (1991), Olsen (2011), and Janin et al. (1992), respectively for B_2, C_2, N_2, T_2, S_3 and T_3. They are selected because: 1) they each offer the possibility to simulate flow hydraulics and sediment transport processes in river channels; 2) they are widely used in fluvial-related research and in engineering applications; 3) they are well documented; and 4) they are available free of charge. Note, however, that C_2 now requires a commercial license, which was not the case when it was used for the current study. The models are used to test for significant differences in simulated flow fields, erosion/deposition patterns and accuracy levels.

In this paper, we use the term “code” to refer to the set of algorithms and solvers embedded in a modelling software package to simulate hydrodynamics and morphodynamics. The term “configuration” refers to the setup of a channel, including its dimensions, shape, substrate characteristics and flow conditions. In this context, a “simulation” denotes a prediction of flow field and/or equilibrium bathymetry obtained by applying a given code to a given configuration.

Channel configurations

The six codes were compared using three sine-generated meandering channels, respectively with a low sinuosity of 1.07 (M_{low}), a medium sinuosity of 1.51 (M_{med}) and a high sinuosity of 3.70 (M_{high}) (Figure 1). For each channel configuration, fixed-flat and mobile beds were considered.

The meandering channel configurations are based on a series of analogue flume experiments. The experimental setup (Figure 1; Table 1), flow and boundary conditions, and generated topographies are described and mapped elsewhere: M_{low} is the numerical version of experiment ME-2 by Hasegawa (1983), with the resulting topography described in Ferreira da Silva and El-Tahawy (2006); M_{med} corresponds to the second run in Binns and Ferreira da Silva (2009); and M_{high} represents the MB-2 experiment described in Termini (2009). The ratio between bed shear stress (measured from the depth-slope product) and Shields critical shear stress ranged between 2.10 and 3.17 at the inlet (Table 1). All experimental data are the result of steady-state runs which lasted sufficiently long to ensure the establishment of an equilibrium bed configuration, based on a constant water surface slope and bed geometry no longer changing through time. Simulated topographic changes (for the mobile bed configurations) are compared to flume results for each numerical code. For the M_{high} configuration, water surface elevations and near-bed velocities were also available from Termini (2009). The latter were compared to the near-bed velocity in the 3D models, but not to the 2D depth-averaged models.

Numerical simulations

The six codes were run for the three flume meander channel configurations (Figure 1) under both fixed-flat and mobile bed conditions, for a total of 36 simulations. Additional simulations were launched to test the sensitivity of the studied codes to variations in key options, sub-models and parameter values.

For each flume configuration and code, a fixed-flat-bed simulation was run to adjust the elevation of the water surface at the inlet so that it is equal to the value at the outlet. This was done by varying bed roughness value (a single value selected for the entire bed) in the 2D simulations, which were similar between the codes (Table 3). This procedure, which is common in CFD modelling (e.g. Bates et al., 1997, Rameshwaran et al., 2013), allows to adjust the energy slope to fit experimental measurements (Vidal et al., 2007). Admittedly, there are limitations to this approach. In particular, 3D models are less sensitive to the choice of Manning's roughness value than 2D models (Lane et al., 1999; 2005). Therefore, the aforementioned calibration procedure failed with S_3 as a change in bed roughness had little effect on the energy slope. In the T_3 simulations, we were unable to configure liquid boundary conditions in a manner such that free surface elevation at the inlet adjusts automatically, and thus depth is also prescribed at the inlet.

As a result, the roughness coefficients used with the 3D codes in this study are those obtained by calibrating the T_2 simulations under the premises that the code T_3 is the three-dimensional version of T_2, that the range of roughness values between the 2D models is narrow, and that the parameter values of the 3D models should be as similar as possible. Another limitation is that, although identical flow conditions were selected between the modelling codes, longitudinally differences exist in predicted depth, velocity, and discharge values, especially between the 2D and 3D codes (Figure S1). Computed discharges are slightly above the values set at the inlet with B_2, N_2 and T_2, but sometimes substantially different with the other codes, e.g. M_{low}-T_3, M_{high}-C_2.

For the mobile-bed simulations, the simulations started from a fixed-flat bed which was allowed to evolve to an equilibrium bathymetry throughout the simulation. Equilibrium bathymetry was assumed to be reached when the mean elevation change, within the zone between $-0.25 \leq \lambda \leq 0.25$ (Figure 1), became small enough that the remaining cumulative change was less than instrument resolution, assumed here equal to 1 mm, to replicate the resolution of topography measurements in Binns and Ferreira da Silva (2009). For each simulation, a plot of cumulative bed elevation change against time was used to estimate the time at which the remaining change was less than the selected threshold value (Table 1). Note that the shape and dimension of dominant bed forms, namely pools and riffles, were stable after each mobile-bed simulation, as in the experiment of Termini (2009). Both the bed development times and the time steps varied substantially amongst the modelling codes and channel configurations, with Courant numbers ($V \cdot \Delta t / \Delta x$, where V is the flow velocity, Δt is the duration of a time step, and Δx is the cell size) generally below unity at the onset of mobile-bed simulations

(Table 2). A Courant number below unity is recommended for good convergence of finite-difference approximations. Note that the calculated values are for average flow conditions and that the modelling code C_2 automatically altered the duration of time steps during each simulation.

Analysis procedure

The evaluation and description of code-code and code-flume discrepancies are derived from visual cues, measurements, and statistical analyses. A set of criteria relevant to fluvial geomorphologists, environmental engineers, ecologists and other river practitioners is employed to describe the predicted flow and equilibrium bathymetry for M_{low}, M_{med} and M_{high}. Channel bathymetries at equilibrium (M_{low}, M_{med} and M_{high}), near-bed velocity magnitudes (M_{high}), and free surface elevations (M_{high}) from the analogue flume experiments were obtained by digitizing the contour lines from the maps published by Hasegawa (1983), Binns and Ferreira da Silva (2009), and Termini (2009). To allow a comparison of simulated flow velocities between 2D and 3D codes, manual depth-averaging of velocities was done in 3D simulation by taking the value at an elevation of 0.6 times the depth below the free surface, a method referred to as the 0.6-depth method (Rantz et al., 1982). Near-bed velocity measurements were taken at a distance of 0.8 cm above the bed in the M_{high} flume experiment over a fixed-flat bed (Termini, 2009). For the comparison with 2D numerical simulations, we estimated near-bed velocities from depth-averaged values using the law of the wall for rough surfaces (Schlichting, 1979), as done by S_3, with a calculated roughness height as $(26 \cdot K_{Strickler})^6$, where $K_{Strickler}$ is the Strickler roughness coefficient (Strickler, 1923). The lateral slope of the free surface was estimated using a linear regression on sample points of the water surface. The bathymetries that developed during the mobile-bed runs and simulations are expressed in terms of absolute and normalized elevation values at equilibrium and in terms of normalized evolution values. Normalized elevations along a cross-section (z_n) are given by $(z - z_{min}) / (z_{max} - z_{min})$, where z = bed elevation at a node, and z_{min}, z_{max} = minimum and maximum bed elevations. This transformation removes the longitudinal bed slope. The extent of the riffles and pools that developed during the mobile-bed flume experiments was derived from a map of normalized evolutions ($\Delta_{z,n}$), given by $(\Delta_z - \Delta_{z,min}) / (\Delta_{z,max} – \Delta_{z,min})$, where Δ_z = bed evolution at any given location and $\Delta_{z,min}$, $\Delta_{z,max}$ = minimum and maximum values measured in the whole flume. Riffles were assumed to be located where $\Delta_{z,n} > 0.75$, and the pools where $\Delta_{z,n} < 0.25$. The point locations of riffles and pools of the bathymetry developed in each numerical simulation correspond to the shallowest and deepest points, respectively, derived from the thalweg and lateral bed profiles.

To avoid spatial autocorrelation problems in statistical analyses (Fortin et al., 1989), 200 test points were randomly selected for each configuration to examine discrepancies amongst and between predicted (numerical simulations) and measured (flume experiments) values. Reduced major axis regression (RMA) is used instead of ordinary least square regression to account for potential errors in both the dependent and independent variables (Hardy et al., 2003; Biron et al., 2007) and to maintain the variance of observations in our predictions (Berterretche et al., 2005). Results of RMA analyses are presented in this paper for the M_{med} but are available as supplementary material for the other two configurations (M_{low} and M_{high}). The relationships associated with a regression slope m not significantly different from 1 at a 0.05 level were identified, as evaluated using two-tailed t-tests where the null hypothesis is that regression slope is equal to 1. As recommended by Paternoster et al. (1998), t-scores were calculated using:

$$t = \frac{b_R - b_{1:1}}{\sqrt{SEb_R^2 - SEb_{1:1}^2}} \quad (1)$$

where SEb_R and $SEb_{1:1}$ are the standards errors associated with b_R and $b_{1:1}$, the regression coefficients of two curves. Here, b_R is the regression slope of the relationship between two datasets, and $b_{1:1} = 1$.

Sensitivity to mesh resolution

A computational mesh structure with a body-fitted coordinate system consisting of quadrilateral cells was employed in all simulations. A sensitivity analysis was performed to determine appropriate horizontal and vertical mesh resolutions to use for the simulations (see supplemental material). Three grid independence tests (Roache et al., 1986; Lane et al., 2005; Biron et al., 2007) were carried out to observe the effects of varying the number of cells in the simulation domain on flow conditions over a fixed-flat-bed for the M_{med} configuration. The procedure, evaluation criteria and results are provided as Supplemental Material. The optimal number of cells was 384 and 32, respectively in the longitudinal and transverse directions, with 6 cells in the vertical direction for the 3D codes. The same horizontal cell size was used for the other two configurations (M_{low} and M_{high}), with the same number of vertical cells for the 3D models (Table 4). Note that the code S_3 automatically adds one row of nodes in each dimension to better account for the effect of solid boundaries on the flow velocity profiles. Finally, despite our intention to use equal vertical cell height with the 3D models, S_3 modified the location of nodes to 0.5, 10, 30, 50, 70, 90 and 100% of flow depth. In order to keep the parameters as similar as possible between the models, the same distribution was used with T_3.

Sensitivity to key model options and sub-models

Our initial intent was to use identical options and sub-models for each numerical simulation. However, this could not be fully achieved since discretization schemes, turbulence models, side wall friction laws, bed load transport formulae, and sediment inflow modes differ between codes (Table 5). A sensitivity analysis was thus conducted with the codes C_2, T_2, and T_3 and channel configuration M_{med} to evaluate whether eventual discrepancies in the flow field and equilibrium bathymetries could be related to differences in options and sub-models.

Spatial discretization. A single scheme is typically implemented in each morphodynamics code, namely finite element (C_2, T_2 and T_3), finite volume (B_2 and S_3) and finite difference (N_2) approaches. In T_2 and T_3, the finite volume scheme is available in scalar mode.

Shear stress and bed roughness. In all codes except S_3, shear stress along an axis i is described by the quadratic friction law, which is a drag coefficient formulation (see Villaret (2010) for a description), whereas S_3 relies on the law of the wall for rough surfaces, i.e. Schlichting (1979) formula, translating a user-provided roughness coefficient to a roughness height using Strickler (1923) formulae. Although bed roughness may be non uniform in natural meandering rivers, varying with local channel curvature and sinuosity (Da Silva, 1999), a single value was assigned to all mesh nodes as 1) detailed spatial variability of bed roughness values was not available for the flume experiments and 2) many modelling studies, even of natural sites, use a single roughness values, particularly for sand-bed cases (e.g. Duan and Julien, 2010; Huang et al., 2014). The choice of the roughness method can affect the simulated flow field and morphodynamics. The Chézy parameterization was found to produce higher velocities, shallower channels, lower-smoother bars, and less accurate morphological predictions than the Nikuradse law (Kasvi et al., 2015). This can be explained by the fact that the former parameterization type does not consider flow velocities (Zeng et al., 2010). S_3 also ignores the terms related to the generation and dissipation of energy due to bed roughness in the governing flow equations. It is well known that the estimated shear stress values vary from one method to another (e.g. Grenier et al., 1995; Wilcock, 1996; Biron et al., 2004; Pasternack et al., 2006). Assuming flow in a straight, rectangular channel with the characteristics listed in Tables 1 and 3, shear stress values predicted by the law of the wall are markedly lower (26% for T_3 and around 53% for B_2, C_2, N_2 and T_2) than those predicted by the quadratic friction law. Scatter in shear stress predictions by hydrodynamic codes was also noticed by Rameshwaran et al. (2013).

Sidewall roughness. Unlike the law of the wall, the quadratic friction law does not take into account sidewall roughness. Lateral friction is nevertheless included in S_3 through the k-ε model (Versteeg and Malalasekera, 1995), which results in steeper lateral velocity gradients than with T_3 due to the smooth sidewalls, and zero velocities near solid boundaries, as in T_3 (Figure 2). A Strickler coefficient of 100 was selected with B_2, T_2, S_3, and T_3 to represent the smooth material of the sidewalls in the analogue flume experiments (unknown for M_{low}; plywood sheet painted with epoxy paint for M_{med}; and clear Plexiglas for M_{high}). The friction law selected in C_2 simulations relies on an empirical slipness coefficient to calculate sidewall velocity strictly based on the value at the adjacent internal node. A value of 0.85 was used with all channel configurations, as recommended by Jia and Wang (2001b) for a numerical simulation with the M_{high} configuration. Although not indicated in the reference manual of N_2, sidewall friction seems to be set to total slip in N_2 due to the lack of a wall effect on lateral velocity profiles.

Turbulence closure. All codes include the k-ε turbulence closure sub-model, except B_2, which only considers molecular viscosity. Despite this, B_2 is included in this study to verify whether a code with limited representation of turbulence structure can simulate flow conditions and bathymetry in an acceptable manner. The bathymetry produced with the k-ε turbulence model exhibits wider point bars than those predicted by Smagorinsky (1963) and constant viscosity closures with a downstream tip disconnected from the sidewall and bed forms with acute delineation and great geometrical regularity (Figure S2).

Bedload transport rate and direction. It is well known that some bed load transport formulae are more accurate than others in specific contexts (Batalla, 1997; Martin and Ham, 2005; Carmelo et al., 2013). In our simulations, we selected Wu et al. (2000) formula when available. Alternatively, the Van Rijn (1984) was selected in T_2/T_3 since it is suited to the range of grain sizes considered in this study. The evaluated codes include algorithms to consider the influence of local bed slope on transport rate (all codes) and direction (only B_2, C_2, and T_2/T_3). The effect of channel curvature on the direction of bed load motion relies on Engelund (1974) in C_2, N_2, and T_2/T_3 to estimate the upslope-inward shearing angle relative to streamline flow direction. In this equation, the angle is proportional to the ratio between flow depth and curvature radius, but the latter is calculated differently in C_2 and N_2 than in T_2/T_3. Note that this option was enabled in C_2 because simulated bathymetries were clearly incorrect when disabled. Our sensitivity analysis reveals that the Meyer-Peter and Müller (1948) formula results in a bathymetry that is almost identical to that produced by Van Rijn (1984). The simulation relying on the total load formula of Engelund and Hansen (1967) is as accurate as the other formulae, and it best predicts the location of pools and point bars even if does not rely on a threshold stress value of particle entrainment.

Sediment inflow rate. B_2, T_2 and T_3 include an option to set the rate of sediment at the inlet equal to the outflow rate, whereas C_2 and S_3 require the inflow rate to be specified. A sediment inflow rate of 0 kg/s was specified with C_2 and S_3 since the simulations launched in S_3 did not converge when using a nonzero, constant rate (estimated with the Meyer-Peter and Müller (1948) formula, assuming a fixed-flat bed) and since it was impossible to predict the equilibrium outflow rate.

Overall, there is a good agreement amongst the bathymetries generated with the different options and sub-models (Figure S2). Taking the regression coefficient as an index of similarity between two predictions, similarity is lowest between turbulence closure sub-models, i.e. k-ε vs. Smagorinsky (1963) or constant viscosity, and between sediment transport formulae, i.e. Engelund and Hansen (1967) vs. Van Rijn (1984) or Meyer-Peter and Müller (1948) (Figure S3). Variations due to lateral friction, sediment inflow, and spatial discretization are less important.

Results

Fixed-flat bed runs

The degree of sinuosity of a meandering channel determines the phase lag between the apex of a meander belt and the location of the zone of maximum velocity, shifting upstream along the inner sidewall with the increase in sinuosity of a fixed-flat bedded channel, almost reaching the cross-over zone in highly sinuous channels (da Silva et al., 2006). Although this trend is well illustrated by S_3, the predicted high-velocity location is fairly similar between T_3 and the depth-averaged models for M_{high} (Figure 2). The evaluated 2D codes, and T_3 to a certain extent, predict a zone of maximum velocity just upstream of the apex, independently of sinuosity, as observed in the experiments of Xu and Bai (2013).

As expected, all codes predict a super-elevation of the free surface along the external sidewall of bends, with mean lateral slopes of 0.97 ± 0.07%, 1.04 ± 0.20% and 2.34±0.66%, respectively for M_{low}, M_{med} and M_{high}, as a result of secondary circulation (Figure 3). However, the degree of agreement between the codes varies with the configuration. For instance, the lateral slopes are nearly identical between the codes in M_{low}, except for T_3, which exhibits an oscillating slope, perhaps due to numerical instability. For M_{med}, the 3D codes predict lateral slopes steeper than with the 2D codes by 52% (S_3) and 30% (T_3). For M_{high}, the free surface elevation for T_3 is more in line with the 2D predictions, whereas the lateral slopes predicted by S_3 is 48% lower than that of the other codes and do not appear to vary with meander configuration. The predictions of free surface elevations are fairly consistent between the 2D codes B_2, C_2, N_2, T_2 for

M_{low} and M_{med}, (except for C_2 in M_{high}) which is to be expected since the calibration procedure consisted in adjusting the slope of the water surface between channel inlet and outlet. For the M_{high} configuration, the agreement with the flume result is also very good, with correlation coefficients of $r \geq 0.88$ (Figure 4). These values can be found in Figure 4b in the cells with white background (associated with the variable free surface elevation) at row 'FL' and columns 'r'. However, the correlation between flume and modelled near-bed velocities is lower ($r \leq 0.47$), with regression slopes much greater than unity with C_2 and T_3 (see the black cells at the row 'FL' and columns 'r' and 'm'), indicating a tendency for an overestimation of near-bed velocities by the codes (Figure 4). The plots associated with these relationships are shown in Figure 4a. For instance, the bottom-left plot presents the relationship between the free surface elevations predicted by T_3 (y variable) against those measured during the analogue flume experiment (x variable) for M_{high}. The top-right plot presents the same relationship for near-bed elevation values.

The regression coefficients for depth-averaged velocity magnitudes between codes reveal some similarities between the 2D codes for M_{low} and M_{med}, but less so for M_{high}, with the exception of N_2 and T_2 which are consistently very similar for all configurations (Figure 5). Surprisingly, a strong similarity ($r = 0.72$, slope not significantly different from 1) is observed between B_2 and S_3 for the M_{high} configuration, whereas this is not the case for less sinuous channels. Although the correlation between the two 3D codes is high (Figure 5; Figures S4-6), the maximum velocity magnitude predicted by T_3 was slightly larger than the values predicted by the other codes for M_{low} (35.4 cm/s in T_3 vs. ≤ 29.2 in the other models) and M_{high} (61.0 cm/s in T_3

vs. ≤ 55.4 cm/s in the other models). However, both 3D codes predict zero velocity zones, whereas C_2 is the only 2D code to predict this (and only for M_{high}). The M_{med} configuration has the highest mean correlation coefficient (0.85), indicating more similarities between simulations for this configuration compared to lower or higher sinuosity (Figure 5d). We also notice a stronger agreement between codes using the same number of dimensions. For instance, the average correlation coefficient is $0.73 \leq r \leq 0.97$ for codes with same dimensionality, but it is of $0.63 \leq r \leq 0.85$ for the other code combinations.

Mobile-bed runs

Meandering channels commonly develop a series of depositional features along the inner bank of the bend at the apex (point bars), scour zones on the opposite bank (pools), and flatter bed morphologies between consecutive pool features (riffles) (Whiting and Dietrich, 1993; Blanckaert, 2010). The six investigated codes indeed predict these features for the three meandering configurations (Figure 6). However, the location, dimensions and shape of geomorphic features differ to the extent that predictions are sometimes opposite, e.g. C_2 vs. T_2 in M_{low}. The bathymetries produced by S_3 involve a wide range of values (Figure 6) and are fairly accurate for M_{med} and M_{high} (Figures 7b-c, 8), which may be attributed to the selection of the Nikuradse law, although N_2 made similar predictions, but did not use Nikuradse.

Velocity predictions in mobile bed simulations (Figure 7d) are, overall, more scattered than on fixed-flat beds (Figures 5d), with mean regression coefficients decreasing from $r = 0.85$ to $r = 0.52$ for M_{med} and from $r = 0.69$ to $r = 0.52$ for M_{high}. In most cases, flow fields that were similar over a fixed-flat bed such as N_2 and T_2

(Figures 5, with *r* values ≥ 0.96) are not as similar on a mobile bed (*r* = 0.61, *r* = 0.23, and *r* = 0.24, respectively for M_{low}, M_{med}, and M_{high}) (Figure 7a-c).

The differences between codes are even greater for bed elevations, with mean regression coefficients of *r* = 0.38, *r* = 0.66, and *r* = 0.43, respectively for M_{low}, M_{med}, M_{high} (Figure 7d). In addition, similar hydraulic predictions between two codes on a fixed-flat bed do not guarantee similar equilibrium morphologies on a mobile bed. For instance, B_2 and N_2 produced similar initial velocity patterns in all configurations (Figures 2, 5a-c), but their equilibrium bathymetries differ considerably (Figures 6, 7a-c). The opposite situation occurs for T_2-T_3, with different velocities leading to similar bathymetries. Finally, the degree of sinuosity affects code similarity.

Overall, the bathymetric predictions were more accurate for the M_{med} configuration. Indeed, the low accuracies obtained under C_2 and S_3 for M_{low} partially contradict the statement of Xu and Bai (2013) that uncertainty of a prediction increases with sinuosity due to greater complexity of bed morphology. Relative to the bathymetries that developed in the flume experiments, N_2 produced the best predictions for all configurations, with regression coefficients of *r* ≥ 0.71 and slopes not significantly different than unity for M_{med} and M_{high} (Figures 7b-c, 8). Some models such as C_2 compare well with flume bathymetry for M_{med}, but the correlation coefficient for the other two configurations is close to zero. For B_2 and T_3, the agreement is high for both M_{low} and M_{med} in terms of the slope, but less so for M_{high}, whereas S_3 and T_2 have a similar regression slope coefficient only for M_{med}. The morphological predictions of transversal bed profiles by the codes B_2 and C_2 differ considerably than the measurements made in the flume at the apex (for M_{low}) and just upstream of the apex (for M_{med} and M_{high})

(Figure 9). The error is less important with the other codes, except with M_{low} for S_3, where the discrepancies are located along the sidewalls just downstream of the apex. These observations are in line with the large discrepancies in cross-sectional profiles found by Xia et al. (2013) between numerical predictions and experimental measurements in a braided natural reach.

The location of the thalweg differs markedly between codes, with the predictions by codes B_2, C_2 (for M_{low} and M_{high}) and S_3 (for M_{low}) being the most different from the measured flume bathymetries (Figure 10). For example, C_2 predicts a riffle where a pool is located at the apex of the meander in M_{high}, whereas it predicts a pool in the riffle located downstream. In general, disparities between predicted morphological features increase with sinuosity. Associated with this are substantial differences in crest location, shape and wave amplitude of longitudinal profiles between the codes, but also between each code and the analogue flume experiments (Figure 11). The shingle bars (series of depositional lobes along the inner bank of a long bend with pools on the adjacent, outer bank) studied by Whiting and Dietrich (1993) and replicated in a flume by Ferreira da Silva and El-Tahawy (2006) and Termini (2009), although formally identified as such only in the latter study, are reproduced by N_2 for M_{med} and M_{high} (Figure 6). The code T_3 predicted oscillations in the longitudinal profile along the pool sections that may, instead, be artefacts of numerical instability due to abrupt increases and drops in bed elevations along the thalweg. Finally, note that N_2 and T_3 match the longitudinal flume profiles relatively well in all configurations.

Discussion

Model options, sub-models and calibration

Our numerical simulations could not be setup in a perfectly identical manner due to the lack of a common set of basic options and sub-models in the evaluated modelling codes (Table 5). Furthermore, it was simply not possible to list and consider all the features involved in each one of the analyzed simulations due to the lack of documentation on some of these features, and since the level of details included in the reference manuals varies between codes. However, sensitivity analyses revealed the limited influence of key options and sub-models on predicted bathymetries for the configuration M_{med}, and thus the variability in predictions can, at least partially, be attributed to code intricacies, such as design and implementation choices.

By ensuring that options, sub-models and parameter values are as similar as possible between the tested codes, recommended settings for a specific code may have been bypassed. In addition, in the absence of detailed hydraulic datasets, only the longitudinal slope of the water surface (e.g. velocity) was adjusted during calibration. We acknowledge that an experienced modeller would likely adjust parameter values differently for a better fit between numerical and flume experiments. However, the main aim for this study was not to numerically replicate flume experiments, but rather to provide explanations and hypotheses for observed differences in terms of hydraulic field and equilibrium bathymetries between modelling codes configured using highly similar initial flow and boundary conditions.

Scatter in predictions and model complexity

Substantial scatter exists in the hydraulic and morphological predictions achieved by the evaluated morphodynamic codes, the degree of accuracy varying with the modelling code, channel configuration and evaluation criterion. Scattering was especially important for M_{low} and M_{high} due to B_2 and C_2 (and S_3 for M_{low}) failing to accurately predict equilibrium bathymetries (Figure 7). With the configurations explored herein, T_3 would best answer a question related to low flow conditions, such as examining the habitat characteristics for aquatic species, due to its ability to predict correctly the location of the thalweg and of the geomorphic features (Figure 10), whilst N_2 could be useful to examine the shape of depositional bars and scour zones (Figure 6). A corollary to the lack of consistency in our simulations is that, since models are used in a range of contexts and disciplines, attributing ranks based on the inconsistent performance of these codes is subjective and pointless. It is also likely that the codes achieving the most accurate predictions in the current study would be less accurate under different channel, hydraulic or sedimentological configurations. A more useful exercise would consist in evaluating the range of applicability of widely used morphodynamics codes to commonly studied river types, e.g. braiding, anastomosing, meandering, and confluence. The options, sub-models and parameter values producing good agreements with datasets from flumes and natural rivers should be identified.

Further investigation helped determine why particular codes do well in a given context and poorly in another, e.g. S_3 in M_{med} and M_{high} vs. M_{low}, according to the regression coefficients for bed elevations (Figure 7). Even though only a small sample of modelling codes was employed in this study, it allowed to identify the options, sub-models and features of a code that are likely to enhance the accuracy of predictions in the context of a meandering river channel.

Given that secondary circulation, bed shear stress, and turbulent kinetic energy are best predicted within a three-dimensional code (Lane et al., 1999; Rameshwaran et al., 2013), it is not surprising that the hydraulic predictions obtained from the 3D codes S_3 and T_3 on a fixed-flat bed outperformed predictions from 2D codes for the configuration M_{high} (Figure 4). We would have expected a similar situation to occur on mobile beds due to the implicit inclusion of secondary flow and sediment circulation in the 3D codes (Rüther and Olsen, 2007). However, the depth-averaged code N_2 was the most accurate for M_{low} and M_{high}, based on the regression coefficients for equilibrium bathymetries (Figure 7a-c). Similarly, the code T_2 was more accurate than S_3 for M_{low} and M_{high}, and as accurate for M_{med}. However, the 3D codes are expected to be more accurate than the 2D codes if suspended transport is activated due to their capacity to correctly simulate morphologies in the presence of strong secondary currents (Ai et al., 2013; Marsooli and Wu, 2014). Nevertheless, given the list of parameters selected (or imposed) for each code (Table 5), and considering the degree of accuracy reached in our sediment simulations, we found little evidence to support the hypothesis that increased code complexity automatically results in increased accuracy. This finding was also reported by Nicholas et al. (2012); in their study, a reduced-complexity model predicted flow field as accurately as 2D and 3D physics-based codes for a natural river reach. Similarly, Kasvi et al. (2015) revealed the preponderant role of the main two-dimensional flow in the development of a meander bend. In that case, perhaps key features of the 3D flow that are included in depth-averaged models, such as helical motion (Begnudelli et al., 2010), would be necessary to achieve accurate predictions, while others would not be essential.

Our results suggest that the effects of local bed slope and channel curvature on transport direction is not critical. The code C_2 includes these algorithms (Table 5), but was the least accurate amongst the evaluated codes for bed topography (Figures 9, 10). Conversely, the most accurate predictions came from N_2, which does not adjust the transport direction based on local bed slope and whose sediment slide algorithm (which ensures that any local slope does not exceed the angle of repose of the bed material) was disabled during our simulations. Similarly, the only code that does not include a turbulence model, B_2, predicts velocity patterns that are comparable to those associated with codes relying on k-ε turbulence closure. Indeed, the predicted patterns are very close to those of C_2, N_2 and T_2 on a fixed-flat bed for M_{low} and M_{med} (Figure 5), and are more accurate than C_2 and S_3 for bed elevations for M_{low} (Figure 7). However, B_2's predictions of equilibrium bathymetry are the worst for M_{med} and second worst for M_{high}, according to the regression coefficients (Figure 7b-c). This suggests that there may be an exception to this observation on complexity vs accuracy, and that a complex turbulence model is indeed required to adequately simulate sediment transport in more sinuous channels.

Bed shear stress and sediment transport are notoriously complex to estimate and prone to large uncertainties (Batalla, 1997; Martin and Ham, 2005; Carmelo et al., 2013; Rameshwaran et al., 2013). Despite this uncertainty, the codes N_2, T_2 and T_3 were fairly accurate in predicting equilibrium bathymetries measured in the three analogue flumes (Figure 7). The set of sub-models and algorithms included in these codes differ from those implemented in the codes B_2, C_2 and S_3. In the former, a sediment supply is present at the inlet, which allows to mimic the condition in a flume with sediment recirculation; channel curvature is estimated and used to calculate transport direction; finite elements are used instead of finite volume; and a formula other than Wu et al. (2000) is used to calculate transport rates (Table 5). Conversely, the presence of a sediment slide algorithm, the consideration of wall friction and the role of bed slope on transport direction do not seem to play a critical role in achieving good predictive accuracy.

Uncertainty of modelling outcomes and purpose of using multiple codes

Assuming that multiple modelling codes are available to examine a phenomenon in a given context, an expert modeller would certainly be able to identify the most appropriate codes to use, based solely on experience and a list of the options and sub-models included in each code. However, assuming that multiple codes offer equivalent options, and in the absence of a validation dataset, it may be impossible to identify the code that is likely to provide the most reliable prediction. Our results suggest that the selection of a code can substantially affect simulated hydraulics and morphologies, and thus the conclusions emerging from a modelling investigation. This is especially true for the codes that include few options (e.g. C_2, N_2), and thus provide fewer opportunities to adjust parameters for a better fit between predicted and observed measurements during calibration. This issue was raised by Jowett and Duncan (2012) who reported that important discrepancies can emerge from the use of 2D and 3D codes due to the challenge of sufficiently calibrating a complex model.

Our results revealed that the accuracy of a modelling code can vary with the simulated environmental context, which suggests that model users should select a code for each specific investigation, regardless of their previous experience with codes. Although there are clear benefits in being able to use multiple codes, we acknowledge that there is a notable duplication of efforts involved in the process. However, enhanced cooperation amongst the developers of a modelling community could facilitate the development of a knowledge base regarding the applicability of fluvial models and help model users to master multiple modelling codes. For instance, single agreed-on formats could be used for basic input files such as bed topography, input flow and sediment discharges. Not only would this help a researcher or practitioner mastering a new code faster, but it would also reduce the list of required pre- and post-processing software. Although most hydrodynamic and morphodynamic models continue to use their own file formats, the International River Interface Cooperative (iRIC) has started addressing this issue by connecting a set of codes through a unique graphical user interface, which demonstrates the need for unity and collaboration in fluvial and coastal processes modelling. Finally, although a set of validation cases is included with most codes, a common set of validation cases in a central repository could serve in cross-validating and improving codes. The simulation and results files from this study are available through Supplemental Material. This provides a first step towards building an exhaustive morphodynamic validation dataset, which hopefully will grow in the future with the addition of other codes and channel configurations.

Conclusion

A series of numerical experiments was undertaken in meandering channels with vertical sidewalls to verify whether flow hydraulics and equilibrium bathymetries would be similar between CFD-based morphodynamic modelling codes subjected to identical initial bed morphologies and very similar initial flow conditions. The numerical codes BASEMENT, CCHE-2D, NAYS, SSIIM-1, and TELEMAC-2D and -3D were used to simulate flow and sediment transport in channels (low, medium and high sinuosity) for which detailed equilibrium bathymetry is available.

Substantial discrepancies were found between the evaluated codes, and between predicted equilibrium bathymetries and observations made in analogue flume experiments. However, no code outperformed the others for all criteria and contexts considered. Indeed, codes that were performing well for a given channel configuration were in many cases not matching well flume bathymetry for a higher or lower sinuosity. This highlights the need to assess codes for more than one channel configuration.

A sensitivity analysis on key modelling options and sub-models revealed the limited influence of turbulence closure methods and bed transport formulae on simulated bed morphologies, relative to that of the choice of a code. Inter-code dissimilarities may be due to the lack of a common method to consider bed and lateral channel roughness and to estimate bed shear stress. Although we only considered a few modelling codes and channel configurations, we found no evidence that a more complex code results in more accurate predictions. In particular, the three-dimensional codes, along with those taking into account local bed slope and channel curvature, were not always accurate.

Uncertainty is an inherent consequence of numerical investigations, which existence can be attributed to process reductionism, scarcity and insufficient quality of real-world data, stochasticity of natural processes, and model structure and parameterization (Uhlenbrook and Sieber, 2005; Carboni et al., 2007). The diversity of modelling codes available should be seen as an opportunity to reduce uncertainty in morphodynamic modelling by using the code that is the most appropriate for any particular context, which involves either knowing a priori which code to use, based on documented benchmark reports, or being able to discover it rapidly through a series of numerical simulations. Although we recognize that practical constraints may conflict with this recommendation, developing, documenting and sharing validation cases between models of the same type would be a first step in this direction, as is done in this study, which gives access to the datasets as Supplemental Material. A central repository holding sample cases and documents regarding the degree of compatibility between modelling codes and channel types would certainly be useful for model users. Another important step would be for a consortium of developers to decide on a single file format to use in morphodynamic models to define cases, topographies and boundary conditions.

Acknowledgements

YY Rousseau is supported by the Fonds de Recherche du Québec - Nature et Technologies (FRQNT) and by the Ontario Graduate (OGS) Scholarship program. PM Biron and MJ Van de Wiel gratefully acknowledge support from the Discovery Grant program of the National Sciences and Engineering Research Council of Canada (NSERC). Comments of four anonymous reviewers are greatly appreciated.

Supporting information

Figure S1. Depth- and width- averaged flow depth (H), velocity (V) and discharge (Q) on a fixed-flat bed for the configurations M_{low}, M_{med}, and M_{high}.

Figure S2. Bathymetries predicted by the models C_2, T_2 and T_3 on a mobile bed for the configuration M_{med} along the central wave.

Figure S3. Linear regression using the reduced major axis technique for bed elevations simulated on a mobile bed in C_2, T_2, and T_3 for M_{med}.

Figure S4. Linear regression using the reduced major axis technique for depth-averaged velocity magnitudes simulated on a fixed-flat bed for the M_{low} configuration.

Figure S5. Linear regression using the reduced major axis technique for depth-averaged velocity magnitudes simulated on a fixed-flat bed for the M_{med} configuration.

Figure S6. Linear regression using the reduced major axis technique for depth-averaged velocity magnitudes simulated on a fixed-flat bed for the M_{high} configuration.

References

Ai C, Jin S, Xing Y. 2013. The influence of suspended load on 3D numerical simulation of flow and bed evolution in a meandering channel bend. *J. Hydraul. Eng.* **139**: 450–455.

Batalla RJ. 1997. Evaluating bed-material transport equations using field measurements in a sandy gravel-bed stream, Arbúcies River, NE Spain. *Earth Surf. Proc. Land.* **22**: 121–130.DOI: 10.1002/(SICI)1096-9837(199702)22:2<121::AID-ESP671>3.0.CO;2-7

Bates BC, Kundzewicz ZW, Wu S, Palutikof JP. 2008. Climate Change and Water. Technical Paper of the Intergovernmental Panel on Climate Change. IPCC Secretariat: Geneva.

Bates PD, Anderson MG, Hervouet J-M, Hawkes JC. 1997. Investigating the behaviour of two-dimensional finite element models of compound channel flow. *Earth Surf. Proc. Land.* **22**: 3–17.

Bates PD, Lane SN, Ferguson RI. 2005. Computational Fluid Dynamics: applications in environmental hydraulics. Wiley: New York.

Begnudelli L, Valiani A, Sanders BF. 2010. A balanced treatment of secondary currents, turbulence and dispersion in a depth-integrated hydrodynamic and bed deformation model for channel bends. *Adv. in Water Resources* **33**: 17–33. DOI: 10.1016/j.advwatres.2009.10.004

Berterretche M, Hudak AT, Cohen WB, Maiersperger T K, Gower ST, Dungan J. 2005. Comparison of regression and geostatistical methods for mapping Leaf Area Index

(LAI) with Landsat ETM+ data over a boreal forest. *Remote Sens. Environ.* **96**: 49–61. DOI: 10.1016/j.rse.2005.01.014

Binns AD (2006). “Time-evolution and stability of the bed in sine-generated meandering streams: An experimental study.” MSc thesis, Queen’s University, Kingston, Canada.

Binns A, Ferreira da Silva A. 2009. On the quantification of the bed development time of alluvial meandering streams. *J. Hydraul. Eng.* **135**(5): 350–360. DOI: 10.1061/(ASCE)HY.1943-7900.0000025

Biron PM, Robson C, Lapointe MF, Gaskin SJ. 2004. Comparing different methods of bed shear stress estimates in simple and complex flow fields, *Earth Surf. Proc. Land.* **29:** 1403–1415. DOI: 10.1002/esp.1111

Biron PM, Haltigin TW, Hardy RJ, Lapointe MF. 2007. Assessing different methods of generating a three-dimensional numerical model mesh for a complex stream bed topography. *Int. J. Comput. Fluid D.* **21**(1): 37–47. DOI: 10.1080/10618560701374411

Blanckaert K. 2010. Topographic steering, flow recirculation, velocity redistribution, and bed topography in sharp meander bends. *Water Resour. Res.* **46**: W09506. DOI: 10.1029/2009WR008303

Brooks HN. 1963. Discussion of “Boundary shear stresses in curved trapezoidal channels” by AT Ippen, PA Drinker. *J. Hydr. Eng. Div.-ASCE* **89**:327–333.

Carboni J, Gatelli D, Liska R, Saltelli A. 2007. The role of sensitivity analysis in ecological modelling. *Ecol. Model.* **203**(1-2): 167–182. DOI: 10.1016/j.ecolmodel.2005.10.045

Carmelo J, Murillo J, García-Navarro P. 2013. Numerical assessment of bed-load discharge formulations for transient flow in 1D and 2D situations. *J. Hydroinform.* **15**(4): 1234–1257. DOI: 10.2166/hydro.2013.153

da Silva AMAF. 1999. Friction factor of meandering flows. *J. Hydraul. Eng.* **125:** 779–783.

da Silva AMF, El-Tahawy T, Tape W. 2006. Variation in flow pattern with sinuosity in sine-generated meandering streams. *J. Hydraul. Eng.* **132**(10): 1003–1014. DOI: 10.1061/(ASCE)0733-9429(2006)132:10(1003)

Darby SE, Van de Wiel MJ. 2003. Models in fluvial geomorphology. In *Tools in fluvial geomorphology*, Kondolf GM, Piégay H (eds). John Wiley & Sons, The Atrium, Southern Gate, Chichester: West Sussex, England; 503–537.

Duan JC, Julien PY. 2010. Numerical simulation of meandering evolution. *J. Hydrol.* **391**, 34–46.

Engelund F. 1974. Flow and bed topography in channel bend. *J. Hydraul. Div. - ASCE* **100**(NHY11): 1631–1648.

Engelund F., Hansen E. 1967. A monograph on sediment transport in alluvial streams. Teknisk Forlag, Denmark.

Fäh R, Müller R, Rousselot P, Vetsch D, Volz C, Vonwiller L, Veprek R, Farshi D. 2011. System Manuals of BASEMENT, Version 2.2. Laboratory of Hydraulics, Glaciology and Hydrology (VAW), ETH Zurich: Switzerland.

Ferreira da Silva, AM, El-Tahawy T. 2006. Location of hills and deeps in meandering streams: an experimental study. In *River Flow*, Ferreira RML, Alves ECTL, Leal JGAB, Cardoso AH (eds). Taylor & Francis Group: London; 1097–1106.

Fischer AM, Weigel AP, Buser CM, Knutti R, Künsch HR, Liniger MA, Schär C, Appenzeller C. 2012. Climate change projections for Switzerland based on a Bayesian multi-model approach. *Int. J. Climatol.* **32**(15): 2348–2371. DOI: 10.1002/joc.3396

Fortin MJ, Drapeau P, Legendre P. 1989. Spatial autocorrelation and sampling design in plant ecology. *Vegetatio* **83**: 209–222. DOI: 10.1007/BF00031693

Franz KJ, Butcher P, Ajami NK. 2010. Addressing snow model uncertainty for hydrologic prediction. *Adv. Water Resour.* **33**(8): 820–832. DOI: 10.1016/j.advwatres.2010.05.004

Galland J-C, Goutal N, Hervouet J-M. 1991. TELEMAC: A new numerical model for solving shallow water equations. *Adv. Water Resour.* **14**(3): 138–148. DOI: 10.1016/0309-1708(91)90006-A

Gregow H, Ruosteenoja K, Pimenoff N, Jylhä K. 2011. Changes in the mean and extreme geostrophic wind speeds in Northern Europe until 2100 based on nine global climate models. *International J. Climatol.* **32**(12): 1834–1846. DOI: 10.1002/joc.2398

Grenier RR Jr, Luettich RA Jr, Westerink JJ. 1995. A comparison of the nonlinear frictional characteristics of two-dimensional and three-dimensional models of a shallow tidal embayment. *J. Geophys. Res.*, **100**(C7): 13,719–13,735. DOI: 10.1029/95JC00841

Ham D, Church M. 2012. Morphodynamics of an extended bar complex, Fraser River, British Columbia. *Earth Surf. Proc. Land.* **37**(10): 1074–1089. DOI: 10.1002/esp.3231

Hardy RJ, Lane SN, Ferguson RI, Parsons DR 2003. Assessing the credibility of a series of computational fluid dynamic simulations of open channel flow. *Hydrol. Process*. **17**: 1539–1560. DOI: 10.1002/hyp.1198

Hasegawa K. 1983. Hydraulic research on planimetric forms, bed topographies and flow in alluvial rivers. Ph.D. thesis. Hokkaido University: Sapporo, Japan.

Huang J, Greimann BP, Randle TJ. 2014. Modelling of meander migration in an incised channel. *Int. J. Sediment. Res.* **29**, 441–453.

Ikeda S. 1982. Lateral bed-load transport on side slopes. *J. Hydr. Eng. Div.-ASCE* **108**(11): 1369–1373.

Janin JM, Lepeintre F, Pechon P. 1992. TELEMAC-3D: a finite element code to solve 3D free surface flow problems (HE-42/92.07). Électricité de France, Laboratoire National d'Hydraulique: Chatou, France.

Jia Y, Wang SSY. 2001a. CCHE2D: Two-dimensional hydrodynamic and sediment transport model for unsteady open channel flows over loose bed (NCCHE-TR-2001-1). National Center for Computational Hydroscience and Engineering, University of Mississippi.

Jia Y, Wang SSY. 2001b. CCHE2D: Verification and validation tests documentation (NCCHE-TR-2001-2). National Center for Computational Hydroscience and Engineering, University of Mississippi.

Jiao Y, Neves R, Jones J. 2008. Models and model selection uncertainty in estimating growth rates of endangered freshwater mussel populations. *Can. J. Fish. Aquat. Sci.* **65**(11): 2389–2398. DOI: 10.1139/F08-141

Jowett IG, Duncan MJ. 2012. Effectiveness of 1D and 2D hydraulic models for instream habitat analysis in a braided river. *Ecol. Eng.* **48**: 92–100. DOI: 10.1016/j.ecoleng.2011.06.036

Kasvi E, Alho P, Lotsari E, Wang Y, Kukko A, Hyyppä H, Hyyppä J. 2015. Two-dimensional and three-dimensional computational models in hydrodynamic and morphodynamic reconstructions of a river bend; sensitivity and functionality. *Hydrol. Process.* **29**:1604–1629.

Koch FG, Flokstra C. 1981. Bed level computations for curved alluvial channels. At *XIXth Congress of the International Association for Hydraulic Research*: New Delhi, India.

Lane SN, Bradbrook KF, Richards KS, Biron PM, Roy AG. 1999. The application of computational fluid dynamics to natural river channels: Three-dimensional versus two-dimensional approaches. *Geomorphology*, **29**: 1–20. DOI: 10.1016/S0169-555X(99)00003-3

Lane SN, Chandler JH, Porfiri K. 2001. Monitoring river channel and flume surfaces with digital photogrammetry. *J. Hydraul. Eng.* **127**:871–877. DOI: 10.1061/(ASCE)0733-9429(2001)127:10(871)

Lane SN, Hardy RJ, Ferguson RI, Parsons DR. 2005. A framework for model verification and validation of CFD schemes in natural open channel flows. In Bates PD, Lane SN, Ferguson RI. Eds.. *Computational Fluid Dynamics: applications in environmental hydraulics*. Wiley: New York, 169–192.

Martin Y, Ham D. 2005. Testing bedload transport formulae using morphologic transport estimates and field data: lower Fraser River, British Columbia. *Earth Surf. Proc. Land.* **30**(10): 1265–1282. DOI: 10.1002/esp.1200

Marsooli R, Wu W. 2014. Three-dimensional numerical modeling of dam-break flows with sediment transport over movable beds. *J. Hydraul. Eng.* **141**:04014066, DOI: 10.1061/(ASCE)HY.1943-7900.0000947

Meyer-Peter E, Müller R. 1948. Formulae for bed-load transport. At *2nd IARH Congress*. Stockholm: Sweden.

Mosselman E. 2012. Modelling sediment transport and morphodynamics of gravel-bed-rivers. In *Gravel bed rivers: processes, tools, environments*, Church MA, Biron P, Roy AG: John Wiley & Sons: New York; 101–115.

Nicholas AP, Sandbach SD, Ashworth PJ, Amsler ML, Best JL, Hardy RJ, Lane SN, Orfeo O, Parsons DR, Reesink AJH, Sambrook Smith GH, Szupiany, R. N. 2012. Modelling hydrodynamics in the Rio Paraná, Argentina: An evaluation and inter-comparison of reduced-complexity and physics based models applied to a large sand-bed river. *Geomorphology* **169-170**: 192–211. DOI: 10.1016/j.geomorph.2012.05.014

Olsen NRB. 2011. A three-dimensional numerical model for simulation of sediment movements in water intakes with multiblock option. Department of hydraulic and environmental engineering, The Norwegian University of Science and Technology.

Pasternack GB, Gilbert AT, Wheaton JM, Buckland EM. 2006. Error propagation for velocity and shear stress prediction using 2D models for environmental management. *J. Hydrol.* **328**: 227–241. DOI: 10.1016/j.jhydrol.2005.12.003

Paternoster R, Brame R, Mazerolle P, Piquero A. 1998. Using the correct statistical test for the equality of regression coefficients. *Criminology* **36**: 859–866. DOI: 10.1111/j.1745-9125.1998.tb01268.x

Rameshwaran P, Naden P, Wilson CAME, Malki R, Shukla DR, Shiono K. 2013. Inter-comparison and validation of computational fluid dynamics codes in two-stage meandering channel flows. *Appl. Math. Model.* **37**(20-21): 8652–8672. DOI: 10.1016/j.apm.2013.07.016

Rantz SE et al. 1982. Measurement and computation of streamflow. Water Supply paper No. 2175: Vols. 1 and 2. U.S. Geological Survey: Washington, D.C.

Rinaldi M, Mengoni B, Luppi L, Darby SE, Mosselman E. 2008. Numerical simulation of hydrodynamics and bank erosion in a river bend. *Water Resour. Res.* **44**(9): W09428. DOI: 10.1029/2008WR007008

Roache PJ, Ghia KN, White FM. 1986. Editorial policy statement on the control of numerical accuracy. *J. Fluid. Eng.-T. ASME* **108**: 2.

Rüther N, Olsen NRB. 2007. Modelling free-forming meander evolution in a laboratory channel using three-dimensional computational fluid dynamics. *Geomorphology* **89**(3-4): 308–319. DOI: 10.1016/j.geomorph.2006.12.009

Schlichting H. 1979. Boundary-layer theory, 7th Edition, trans. by J. Kestin. McGraw-Hill: New York and London.

Shimizu Y, Inoue T, Hamaki M, Iwasaki T. 2013. Nays2D solver manual. iRIC Project.

Smagorinsky J. 1963. General circulation experiments with the primitive equations. *Monthly Weather Review* **91**: 99–164.

Strickler A. 1923. Beiträge zur Frage der Geschwindigkeitsformel und der Rauhigkeitszahlen fur Ströme, Kanäle und Geschlossene Leitungen, Berna.

Talmon AM, Van Mierlo MCLM, Struiksma N. 1995. Laboratory measurements of the direction of sediment transport on transverse alluvial-bed slopes. *J. Hydraul. Res.* **33**(4): 495–517.

Termini D. 2009. Experimental observations of flow and bed processes in large-amplitude meandering flume. *J. Hydraul. Eng.* **135**(7): 575–587. DOI: 10.1061/(ASCE)HY.1943-7900.0000046

Uhlenbrook S, Sieber A. 2005. On the value of experimental data to reduce the prediction uncertainty of a process-oriented catchment model. *Environ. Modell. Softw.* **20**: 19–32. DOI: 10.1016/j.envsoft.2003.12.006

Van Rijn LC. 1984. Sediment transport, part I: bed load transport. *J. Hydraul. Eng.* **110**(10): 1431–1456.

Van Rijn LC. 1989. Handbook: sediment transport by current and waves (H 461). Delft Hydraulics: Netherlands.

Versteeg HK, Malalasekera W. 1995. Turbulence and its modelling. In *An introduction to computational fluid dynamics*, Versteeg HK, Malalasekera W. Pearson Education Limited: Essex, England; 41–84.

Vidal J-P, Moisan S, Faure J-B, Dartus D. 2007. River model calibration, from guidelines to operational support tools. *Environ. Modell. Softw.* **22**: 1628–1640. DOI: 10.1016/j.envost.2006.12.003

Villaret C. 2010. SISYPHE 6.0 User manual (H-P73-2010-01219-FR). National hydraulic and environment laboratory, EDF R&D: Chatou, France.

Whiting PJ, Dietrich WE. 1993. Experimental studies of bed topography and flow patterns in large-amplitude meanders. *Water Resour. Res.* **29**(11): 3615–3622. DOI: 10.1029/93WR01756

Wilcock PR, 1996. Estimating local shear stress from velocity observations, *Water Resour. Res*. **32**: 3361–3366. DOI: 10.1029/96WR02277

Wu W, Wang SSY, Jia Y. 2000. Nonuniform sediment transport in alluvial rivers. *J. Hydraul. Res.* **38**(6): 427–434.

Xia J, Wang Z, Wang Y, Yu X. 2013. Comparison of morphodynamic models for the Lower Yellow River. *J. Am. Water Resour. As.* **49**(1): 114–131. DOI: 10.1111/jawr.12002

Xu D, Bai Y. 2013. Experimental study on the bed topography evolution in alluvial meandering rivers with various sinuousnesses. *J. Hydro Environ. Res.* **7**: 92–102.

Zeng J, Constantinescu G, Weber L. 2010. 3D calculations of equilibrium conditions in loose-bed open channels with significant suspended sediment load. *J. Hydraul. Eng.* **136**:557–571. DOI: 10.1061/(ASCE)HY.1943-7900.0000213

List of figures

different from the 1:1 slope. The labels 'y/x' indicate the order of comparison, where y is the dependent variable and x the independent variable.

Figure 5. Comparison of simulated depth-averaged velocity magnitudes on a fixed-flat bed for a) M_{low}, b) M_{med}, and c) M_{high}. RMA regression is carried out on a sample of 200 points located along the central wave, i.e. -0.5 < λ < 0.5 in Figure 1. Values in gray cells are not significantly different from the 1:1 slope. d) Mean coefficient values.

Figure 6. Bathymetries predicted by the numerical simulations versus those developed in the analogous flume experiments, i.e. on mobile bed, along the central wave, i.e. -0.5 < λ < 0.5 in Figure 1. Minimum and maximum values are displayed below each map. The measured and predicted locations of the shingle bars along the external sidewall of meander bends are indicated with black dots.

Figure 7. RMA regression parameters from the comparison of simulated depth-averaged velocity magnitudes (black background) and bed elevations (white background) on a mobile bed for a) M_{low}, b) M_{med}, and c) M_{high}. RMA regression is carried out on a sample of 200 points located along the central wave, i.e. -0.5 < λ < 0.5 in Figure 1. The dataset FL corresponds to the flume experiment by Termini (2009). Dashed lines show 1:1 agreement whereas full lines correspond to the regression slope. Values in gray cells are not significantly different from the 1:1 slope. d) Mean coefficient values.

Figure 8. Comparison of simulated depth-averaged velocity magnitudes (black background) and bed elevations (white background) on a mobile bed for the configuration M_{high}. RMA regression is carried out on a sample of 200 points located along the central wave, i.e. -0.5 < λ < 0.5 in Figure 1. The dataset FL corresponds to the

flume experiment by Termini (2009). Dashed lines show 1:1 agreement whereas full lines correspond to the regression slope. Values in gray cells are not significantly different from the 1:1 slope.

Figure 9. Differences between predicted and measured normalized bed elevations, presented in number of standard deviations, σ. Minimum and maximum values are displayed beside each map.

Figure 10. Location of the thalweg, pools and riffles for the flume experiments and numerical simulations along the central wave, i.e. $-0.5 < \lambda < 0.5$ in Figure 1, for a) M_{low}, b) M_{med}, and c) M_{high}. Symbols represent the shallowest and deepest points, respectively, for the riffles and pools, and were derived from the longitudinal (along the thalweg) and lateral bed profiles. The full extent of the riffle and pool features is shown for the flume data only.

Figure 11. Longitudinal profiles obtained from the flume experiments and predicted in the numerical simulations for the three meandering configurations on mobile beds. 'S' represents the downslope longitudinal slope computed from riffle-to-riffle elevation differences. The correlation coefficient 'r' indicates the level of agreement between the predicted and measured profiles.

List of tables

Table 1. Flow and boundary conditions for each channel configuration. Each sine-generated channel consists of two waves located between two two-meter straight sections.

Config.	σ	L (m)	B (cm)	H (cm)	B/H	Q (l/s)	S (%)	d_{50} (mm)	Shear stress ratio
M_{low}	1.07	8.00	30	2.60	11.5	1.87	0.333	0.43	2.36
M_{med}	1.51	19.20	80	4.14	19.3	9.50	0.400	0.65	3.17
M_{high}	3.70	27.30	50	3.00	16.7	7.00	0.371	0.65	2.10

σ = sinuosity; L = total flume length; B = channel width; *H* = depth at inlet and outlet; *Q* = flow discharge at inlet; S = longitudinal slope; d_{50} = median grain size diameter. The shear stress ratio is the ratio of shear stress (τ = ρ g R S, where ρ is mass density of water, g is acceleration due to gravity and R is hydraulic radius) over critical shear stress ($\tau_c = \theta_c (\gamma_s - \gamma)\, d_{50}$, where θ_c is taken as 0.044, γ_s is weight density of sediment in kg/m^3 and γ is weight density of water in kg/m^3 and d_{50} is in m.

Table 2. Simulation time and initial duration of a time step at the onset of mobile-bed simulations, and theoretical Courant number values on rectangular beds with uniform hydraulic simulations.

Code	Time to reach equilibrium (hours:minutes)			Initial time step (ms)			Courant number		
	M_{low}	M_{med}	M_{high}	M_{low}	M_{med}	M_{high}	M_{low}	M_{med}	M_{high}
FL	4:00	1:22	2:30	-	-	-	-	-	-
B_2	2:31	307:47	66:30	100	100	100	0.64	0.76	1.24
C_2	125:12	131:15	102:55	10	10	10	0.06	0.08	0.12
N_2	134:17	42:19	22:01	1	1	2.5	0.01	0.01	0.03
T_2	5:15	54:08	2:41	10	10	10	0.06	0.08	0.12
S_3	43:48	27:23	99:24	100	100	100	0.64	0.76	1.24
T_3	30:42	43:08	17:01	50	100	100	0.32	0.76	1.24

Table 3. Bed roughness values (Strickler coefficients) used in adjusting the slope of the water surface between the inlet and outlet of each channel.

Configuration	Model			
	B_2	C_2	N_2	$T_2/T_3/S_3$
M_{low}	49.50	50.50	47.94	47.67
M_{med}	38.75	39.00	38.07	38.12
M_{high}	86.00	92.18	79.94	80.12

Table 4. Number of cells and mean cell size of the numerical meshes in the longitudinal (i), lateral (j) and vertical (k) directions.

Model	**Number of cells**				**Mean cell size (cm)**		
	i	**j**	**k**	**i·j·k**	**i**	**j**	**k**
$\mathbf{M_{low}}$							
B_2, C_2, N_2, T_2	161	12	1	1,932	4.99	2.50	2.60
S_3	162	13	6	12,636	4.96	2.31	0.43
T_3	161	12	6	11,592	4.99	2.50	0.43
$\mathbf{M_{med}}$							
B_2, C_2, N_2, T_2	384	32	1	12,288	4.99	2.50	4.14
S_3	385	33	6	76,230	4.98	2.42	0.69
T_3	384	32	6	73,728	4.99	2.50	0.69
$\mathbf{M_{high}}$							
B_2, C_2, N_2, T_2	545	20	1	10,900	5.00	2.50	3.00
S_3	546	21	6	68,796	4.99	2.38	0.50
T_3	545	20	6	65,400	5.00	2.50	0.50

Table 5. Selected options, sub-models and parameter values in the numerical simulations.

Criteria	B_2 – BASEMENT	C_2 – CCHE-2D	N_2 – NAYS-2D	T_2/T_3 – TELEMAC	S_3 – SSIIM-1
Flow hydraulics					
Governing equations	Shallow-water	Shallow-water	Shallow-water	Shallow water (2D) Navier Stokes (3D)	Navier-Stokes
Spatial discretization[1]	FVM	FEM	FDM	FEM	FVM
Advection	Upwind	Upwind	Upwind	Upwind	Upwind
Turbulence model	None	k-ε	k-ε	k-ε	k-ε[2]
Friction law (bed)	Quadratic-Manning	Quadratic-Manning	Quadratic-Manning	Quadratic-Manning	Wall law-Manning
Friction law (walls)	Quadratic-Manning	Coefficient	None	Quadratic-Manning	Quadratic-Manning
Sediment transport					
Bed load formula[3]	TF_{WWJ}	TF_{WWJ}	TF_{MPM}	TF_{VR}	TF_{WWJ}
Magnitude=f(slope)	Van Rijn (1989) & Ikeda (1982)	Van Rijn (1989)	Hasegawa (1983) & Engelund (1974)	Koch and Flokstra (1981)	Brooks (1963)
Direction=f(slope)	Perpendicular to main flow direction	Talmon et al. (1995)	No	Koch and Flokstra (1981)	No
Direction=f(curvature)	No	Engelund (1974)	Engelund (1974)	Engelund (1974)	No
Sediment slide[4]	No	Yes	No	Yes	No
Inflow rate	Variable[5]	None	Variable[5]	Variable[5]	No

[1]Equations: finite element (FEM), finite volume (FVM), finite difference (FDM). [2]The implementation of the k-ε turbulence model in S_3 does not take account of turbulent energy and dissipation due to bed friction. [3]Valid mean grain size (d_{50}) ranges for the bedload formulae are: $2 < d_{50} < 50$mm with Meyer-Peter and Müller (1948) (TF_{MPM}); $0.2 < d_{50} < 2$mm with Van Rijn (1984) (TF_{VR}); and $0.088 < d_{50} < 28.7$mm with Wu el al. (2000) (TF_{WWJ}). [4]This algorithm ensures that no slope exceeds the angle of repose of the bed material. [5]The amount of sediment crossing the upstream boundary is equal to the amount leaving the first cell.

Sensitivity of simulated flow fields and bathymetries in meandering channels to the choice of a morphodynamic model

Supporting Information

Yannick Y. Rousseau[1], Pascale M. Biron[2], Marco J. Van de Wiel[3]

Methodology

Sensitivity to mesh resolution

A computational mesh structure with a body-fitted coordinate system consisting of quadrilateral cells was employed in all simulations. The sensitivity of models B_2, T_2 and S_3 to the number of horizontal cells was assessed using mesh H_A (679 cells, i.e. 97x7), H_B (3281 cells, i.e. 193x17), H_C (12,705 cells, i.e. 385x33), and H_D (49,985 cells, i.e. 769x65). The number of cells in the vertical direction was six when varying horizontal resolution in S_3. The sensitivity of T_3 to a change in vertical resolution was evaluated by launching simulations with meshes V_2, V_4, V_6, V_8, V_{10} and V_{12}, the subscript indicating the number of vertical cells.

Three grid independence tests (Roache et al., 1986; Lane et al., 2005; Biron et al., 2007) were carried out through a series of fixed-flat-bed simulations for the M_{med} configuration (Figure 1). The first test compared the predicted minimum and maximum flow depths and velocity magnitudes (along the x-, y- and z-axes) with the values obtained with the finest horizontal mesh H_D. A difference of less than 10% was achieved with meshes H_B (for all variables) and V_6 (except for minimum depth and velocity along the x-axis). In the second test, grid convergence indices were calculated at 200 point locations, selected randomly within the zone delimited by $-1.0 \leq \lambda \leq 1.0$ (see Figure 1), and compared between the mesh resolutions for the depth and velocity variables. Using meshes H_B and V_8 maximized the horizontal and vertical grid convergence indices (except for vertical velocity). In the third test reduced-major axis regression was computed for the same 200 locations, comparing flow depth and velocity predictions between mesh resolutions. A correlation coefficient larger than 0.95 was obtained for meshes H_B, H_C and H_D (all variables) and when using at least 6 vertical cells (except for velocity in the vertical direction). The horizontal and vertical mesh resolutions used to carry out the numerical experiments were those which performed well in the three tests for most codes and variables: meshes H_C and V_6.

References

Biron PM, Haltigin TW, Hardy RJ, Lapointe MF. 2007. Assessing different methods of generating a three-dimensional numerical model mesh for a complex stream bed topography. *Int. J. Comput. Fluid D.* **21**(1): 37–47. DOI: 10.1080/10618560701374411

Boussinesq J. 1872. Théorie des ondes et des remous qui se propagent le long d'un canal rectangulaire horizontal, en communiquant au liquide contenu dans ce canal des vitesses sensiblement pareilles de la surface au fond. *J. Math. Pures Appl.* **17**:55–108.

Boussinesq JV. 1871. Théorie générale des mouvements qui sont propagés dans un canal rectangulaire horizontal. *C. R. Acad. Sc.* **73**: 256–260.

Engelund F., Hansen E. 1967. A monograph on sediment transport in alluvial streams. Teknisk Forlag, Denmark.

Lane SN, Hardy RJ, Ferguson RI, Parsons DR. 2005. A framework for model verification and validation of CFD schemes in natural open channel flows. In Bates PD, Lane SN, Ferguson RI. Eds. *Computational Fluid Dynamics: applications in environmental hydraulics*. Wiley: New York, 169–192.

Meyer-Peter E, Müller R. 1948. Formulae for bed-load transport. At *2nd IARH Congress*. Stockholm: Sweden.

Roache PJ, Ghia KN, White FM. 1986. Editorial policy statement on the control of numerical accuracy. *J. Fluid. Eng.-T. ASME* **108**: 2.

Smagorinsky J. 1963. General circulation experiments with the primitive equations. *Monthly Weather Review* **91**: 99–164.

Van Rijn LC. 1984. Sediment transport, part I: bed load transport. *J. Hydraul. Eng.* **110**(10): 1431–1456.

List of figures

Figure S1. Depth- and width- averaged flow depth (H), velocity (V) and discharge (Q) on a fixed-flat bed for the configurations M_{low}, M_{med}, and M_{high}. The view was cropped in the M_{low} plots due to larger values produced by T_3, with maximum values of 2.94 cm, 30.0 cm/s and 2.30 l/s, respectively for H, V, and Q; and a minimum value of 20.5 cm/s for V.

Figure S2. Bathymetries predicted by the models C_2, T_2 and T_3 on a mobile bed for the configuration M_{med} along the central wave, i.e. $-0.5 < \lambda < 0.5$ in Figure 1. The predictions on the first row correspond to the settings described in Table 5. The subsequent rows show the bathymetries obtained by altering lateral friction, sediment inflow rate, spatial discretization, turbulence closure, or bed load transport formula. The acronyms are explained in Figure S2. The selected inflow rate is 1.66 g/m/s, which is the outflow rate simulated by C_2 at the onset of the mobile bed simulation. The map identified as FL corresponds to the analogue flume experiment. Minimum and maximum values are displayed below each map.

Figure S3. Linear regression using the reduced major axis technique for bed elevations simulated on a mobile bed in a) C_2, b) T_2, and c) T_3 for M_{med}. The predictions using the settings described in Table 5 are compared to predictions obtained by altering lateral friction, sediment inflow rate, spatial discretization, turbulence closure, or bed load transport formula.

Figure S4. Linear regression using the reduced major axis technique for depth-averaged velocity magnitudes simulated on a fixed bed for the M_{low} configuration. RMA regression is carried out on a sample of 200 points located along the central wave, i.e. $-0.5 < \lambda < 0.5$ in Figure 1. Dashed lines show 1:1 agreement whereas full lines correspond to the regression slope. Highlighted values are not significantly different from the 1:1 slope. The labels 'y/x' indicate the order of comparison, where y is the dependent variable and x the independent variable.

Figure S5. Linear regression using the reduced major axis technique for depth-averaged velocity magnitudes simulated on a fixed bed for the M_{med} configuration. RMA regression is carried out on a sample of 200 points located along the central wave, i.e. $-0.5 < \lambda < 0.5$ in Figure 1. Dashed lines show 1:1 agreement whereas full lines correspond to the regression slope. Highlighted values are not significantly different from the 1:1 slope. The labels ‘y/x’ indicate the order of comparison, where y is the dependent variable and x the independent variable.

Figure S6. Linear regression using the reduced major axis technique for depth-averaged velocity magnitudes simulated on a fixed bed for the M_{high} configuration. RMA regression is carried out on a sample of 200 points located along the central wave, i.e. $-0.5 < \lambda < 0.5$ in Figure 1. Dashed lines show 1:1 agreement whereas full lines correspond to the regression slope. Highlighted values are not significantly different from the 1:1 slope. The labels ‘y/x’ indicate the order of comparison, where y is the dependent variable and x the independent variable.

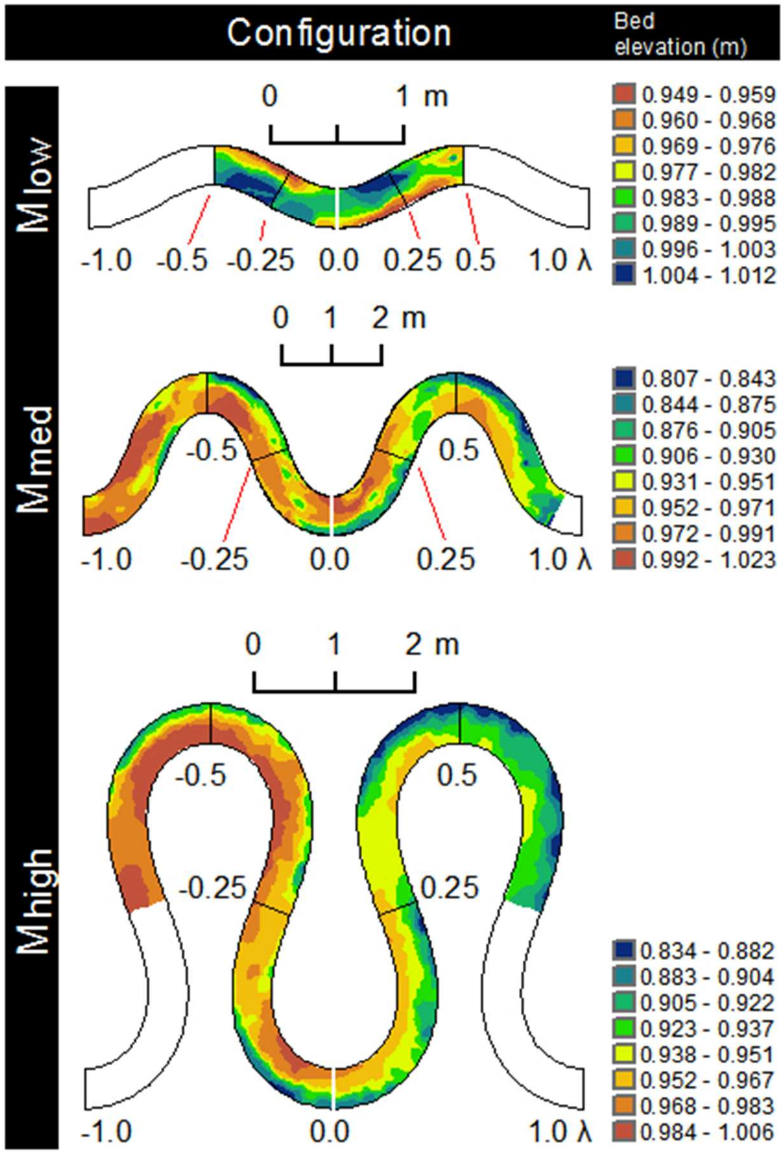

76x110mm (150 x 150 DPI)

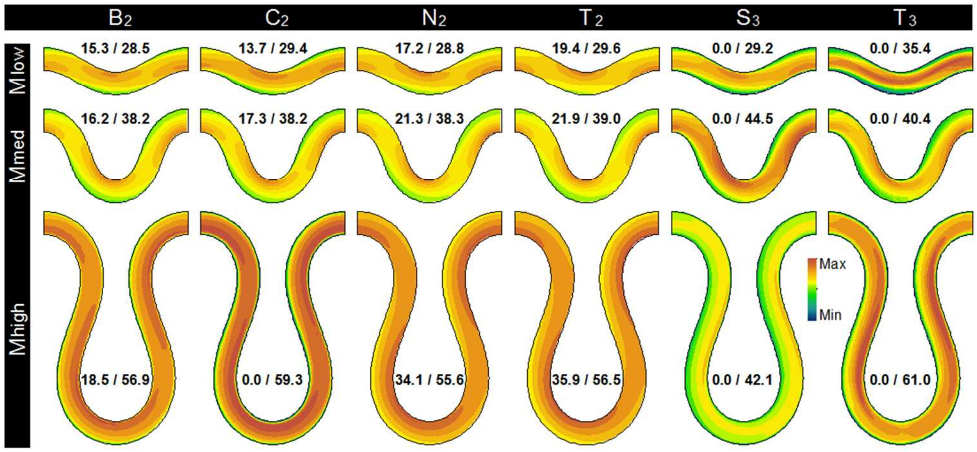

191x89mm (150 x 150 DPI)

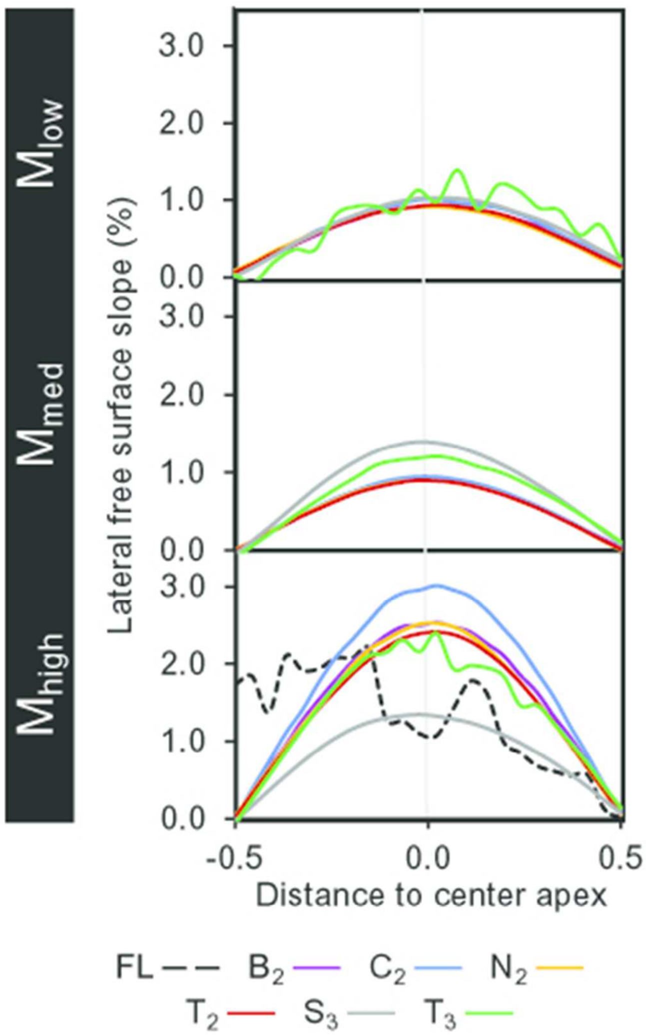

58x90mm (150 x 150 DPI)

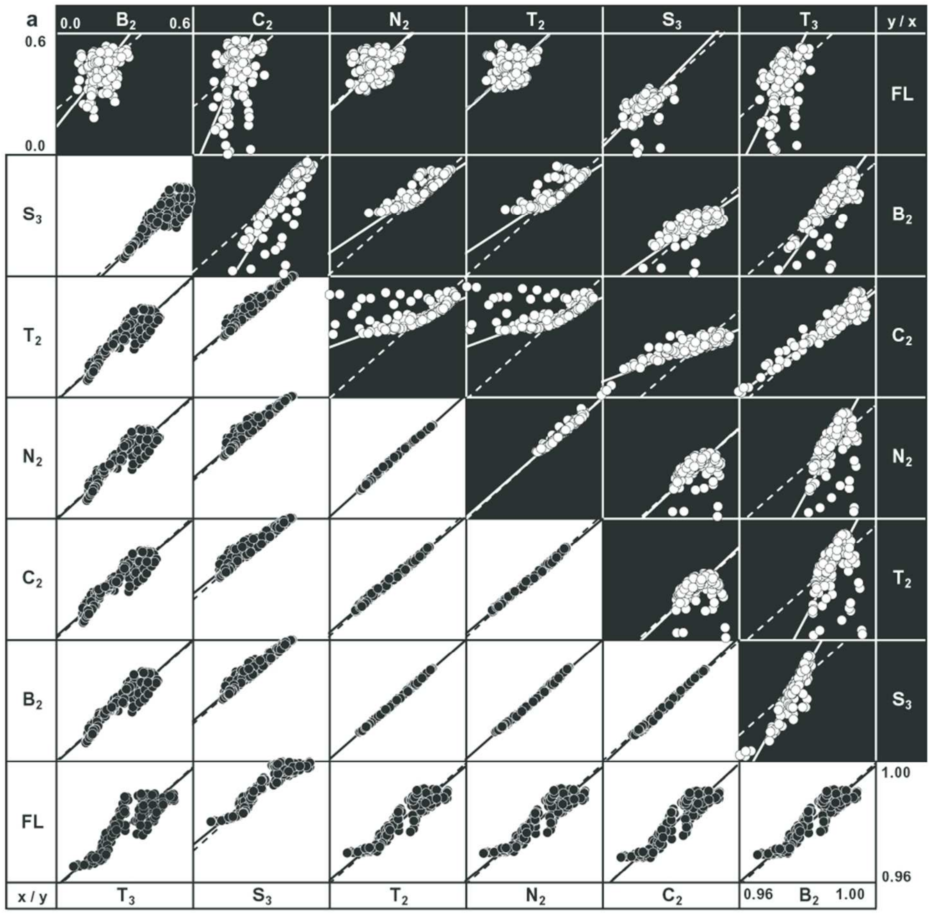

b

	r	m	b	r	m	b	r	m	b	r	m	b	r	m	b	r	m	b	
	B_2			C_2			N_2			T_2			S_3			T_3			y / x
	0.31	1.43	0.13	0.31	2.59	-0.09	0.28	1.07	0.21	0.20	1.05	0.21	0.47	1.12	0.03	0.38	2.23	-0.07	FL
S_3	0.90	1.08	-0.09	0.83	1.81	-0.33	0.88	0.75	0.11	0.81	0.73	0.11	0.68	0.78	-0.08	0.81	1.56	-0.28	B_2
T_2	0.91	**1.03**	-0.03	0.99	0.95	0.06	0.52	0.41	0.25	0.38	0.41	0.25	0.89	0.43	0.07	0.94	0.86	0.01	C_2
N_2	0.91	**1.03**	-0.03	0.98	0.95	0.06	1.00	**1.00**	0.00	0.98	0.98	0.01	0.41	1.05	-0.19	0.52	2.08	-0.51	N_2
C_2	0.92	**0.96**	0.04	0.98	0.89	0.12	1.00	0.94	0.06	1.00	0.94	0.06	0.28	1.07	-0.19	0.40	2.13	-0.52	T_2
B_2	0.92	**1.02**	-0.02	0.98	0.95	0.06	1.00	**1.00**	0.00	1.00	**1.00**	0.00	1.00	1.06	-0.06	0.92	1.99	-0.13	S_3
FL	0.88	**0.97**	0.02	0.93	0.90	0.11	0.93	**0.95**	0.05	0.92	0.95	0.05	0.92	**1.01**	-0.01	0.93	**0.95**	0.05	
x / y	T_3			S_3			T_2			N_2			C_2			B_2			

Linear regression —— 1:1 slope — — Data point ●

r = Correlation coefficient; m = Regression slope coefficient; b = Regression y-intercept coefficient

175x224mm (150 x 150 DPI)

a

y / x	C_2 r	C_2 m	C_2 b	N_2 r	N_2 m	N_2 b	T_2 r	T_2 m	T_2 b	S_3 r	S_3 m	S_3 b	T_3 r	T_3 m	T_3 b
B_2	0.93	1.29	-0.06	0.95	0.96	0.01	0.89	0.89	0.02	0.84	2.18	-0.30	0.70	3.27	-0.56
C_2				0.87	0.74	0.06	0.72	0.70	0.07	0.90	1.69	-0.19	0.84	2.55	-0.40
N_2							0.96	0.94	0.01	0.71	2.28	-0.32	0.53	3.43	-0.60
T_2										0.55	2.43	-0.36	0.35	3.66	-0.65
S_3													0.89	1.50	-0.11

b

y / x	C_2 r	C_2 m	C_2 b	N_2 r	N_2 m	N_2 b	T_2 r	T_2 m	T_2 b	S_3 r	S_3 m	S_3 b	T_3 r	T_3 m	T_3 b
B_2	0.99	1.01	0.00	0.97	0.92	0.02	0.95	0.91	0.03	0.83	2.06	-0.26	0.79	1.87	-0.25
C_2				0.96	0.91	0.02	0.94	0.89	0.03	0.86	2.03	-0.26	0.82	1.84	-0.25
N_2							1.00	0.98	0.00	0.72	2.24	-0.31	0.64	2.03	-0.30
T_2										0.68	2.27	-0.32	0.60	2.07	-0.30
S_3													0.96	0.91	-0.01

c

y / x	C_2 r	C_2 m	C_2 b	N_2 r	N_2 m	N_2 b	T_2 r	T_2 m	T_2 b	S_3 r	S_3 m	S_3 b	T_3 r	T_3 m	T_3 b
B_2	0.85	1.91	-0.41	0.87	0.71	0.13	0.78	0.69	0.14	0.72	1.03	-0.15	0.82	1.76	-0.39
C_2				0.54	0.37	0.29	0.38	0.36	0.29	0.91	0.54	0.08	0.95	0.92	-0.01
N_2							0.98	0.97	0.01	0.44	1.44	-0.34	0.51	2.47	-0.72
T_2										0.29	1.48	-0.35	0.38	2.54	-0.74
S_3													0.93	1.72	-0.14

d

M_{low} r	M_{low} m	M_{low} b	M_{med} r	M_{med} m	M_{med} b	M_{high} r	M_{high} m	M_{high} b	Codes
0.89	0.92	0.02	0.97	0.94	0.02	0.73	0.84	0.07	2D vs. 2D
0.89	1.50	-0.11	0.96	0.91	-0.01	0.93	1.72	-0.14	3D vs. 3D
0.68	2.68	-0.42	0.74	2.05	-0.28	0.63	1.52	-0.33	2D vs. 3D
0.77	1.90	-0.22	0.85	1.53	-0.14	0.69	1.26	-0.15	Any

r = Correlation coefficient; m = Regression slope coefficient; b = Regression y-intercept coefficient

146x119mm (150 x 150 DPI)

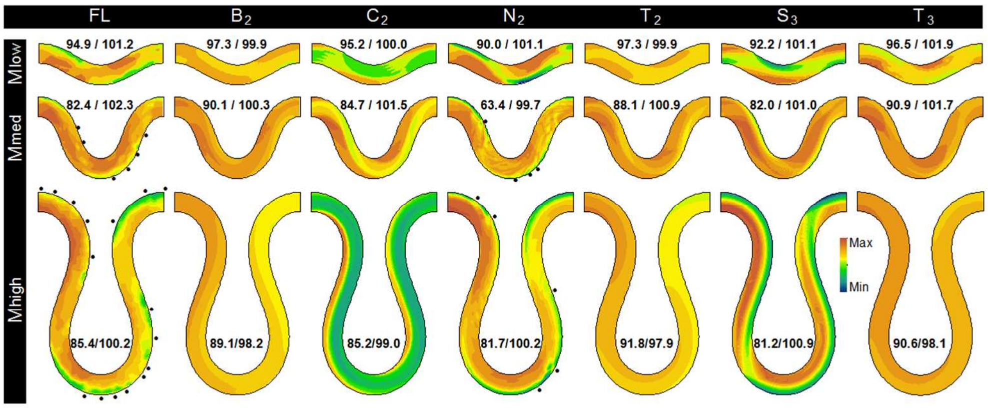

219x92mm (150 x 150 DPI)

a	r	m	b	r	m	b	r	m	b	r	m	b	r	m	b	r	m	b	
	B_2			C_2			N_2			T_2			S_3			T_3			y / x
S_3	-0.26	-0.46	1.44	0.91	2.17	-0.29	0.54	2.11	-0.30	0.97	1.28	-0.07	0.93	2.74	-0.48	0.60	2.81	-0.44	B_2
T_2	0.65	2.05	-1.03	0.29	4.40	-3.36	0.74	0.97	-0.01	0.92	0.59	0.10	0.90	1.26	-0.11	0.76	1.30	-0.06	C_2
N_2	0.65	0.46	0.54	-0.10	-0.98	1.94	0.61	0.22	0.77	0.61	0.61	0.11	0.53	1.30	-0.10	0.53	1.33	-0.04	N_2
C_2	0.00	-0.77	1.73	0.81	1.65	-0.63	0.48	0.38	0.62	0.00	-1.69	2.62	0.94	2.14	-0.33	0.60	2.20	-0.28	T_2
B_2	0.03	1.90	-0.89	0.89	4.09	-3.06	0.59	**0.93**	0.07	0.26	4.17	-3.13	0.84	2.47	-1.47	0.72	1.03	0.06	S_3
FL	0.72	0.71	0.28	0.06	1.54	-0.54	0.68	0.35	0.64	0.85	1.57	-0.56	0.05	**0.93**	0.05	0.35	0.38	0.62	
y / x	T_3			S_3			T_2			N_2			C_2			B_2			

b	r	m	b	r	m	b	r	m	b	r	m	b	r	m	b	r	m	b	
	B_2			C_2			N_2			T_2			S_3			T_3			y / x
S_3	0.59	0.55	0.43	0.36	1.36	-0.13	-0.07	-0.51	0.32	0.72	1.47	-0.13	0.61	1.45	-0.15	0.59	0.96	0.01	B_2
T_2	0.68	0.87	0.13	0.81	1.59	-0.55	0.37	0.37	0.13	0.66	1.08	0.01	0.73	1.07	-0.01	0.73	0.71	0.10	C_2
N_2	0.66	0.54	0.46	0.66	**0.97**	0.05	0.62	0.61	0.38	0.23	2.90	-0.35	0.25	2.87	-0.37	0.34	1.90	-0.14	N_2
C_2	0.69	0.47	0.52	0.71	0.85	0.17	0.85	0.54	0.45	0.50	**0.88**	0.12	0.88	0.99	-0.02	0.66	0.65	0.09	T_2
B_2	0.40	**1.16**	-0.15	0.77	2.09	-1.05	0.74	1.32	-0.32	0.48	2.16	-1.14	0.72	2.45	-1.43	0.71	0.66	0.00	S_3
FL	0.77	0.56	0.42	0.64	**1.02**	-0.02	0.64	0.65	0.33	0.71	**1.05**	-0.08	0.62	1.20	-0.22	0.50	0.49	0.49	
y / x	T_3			S_3			T_2			N_2			C_2			B_2			

c	r	m	b	r	m	b	r	m	b	r	m	b	r	m	b	r	m	b	
	B_2			C_2			N_2			T_2			S_3			T_3			y / x
S_3	0.41	0.20	0.76	0.42	1.54	-0.48	0.20	1.32	-0.24	0.91	0.59	0.19	0.34	1.63	-0.44	0.72	1.06	-0.05	B_2
T_2	0.99	1.15	-0.14	0.41	5.65	-4.41	0.57	0.85	0.17	0.61	0.38	0.38	0.77	1.06	0.07	0.36	0.69	0.28	C_2
N_2	0.64	0.33	0.64	0.73	1.62	-0.59	0.64	0.29	0.68	0.24	0.44	0.30	0.62	1.24	-0.14	0.44	0.81	0.14	N_2
C_2	0.06	0.25	0.72	0.25	1.24	-0.17	0.07	0.22	0.75	-0.10	-0.77	1.63	0.48	2.79	-0.98	0.57	1.82	-0.40	T_2
B_2	0.69	**1.12**	-0.11	0.30	5.50	-4.28	0.69	**0.97**	0.02	0.20	3.40	-2.28	0.51	4.43	-3.32	0.49	0.65	0.24	S_3
FL	0.70	0.34	0.63	0.65	1.67	-0.64	0.67	0.30	0.67	0.81	**1.03**	-0.03	-0.08	-1.34	2.16	0.29	0.30	0.66	
y / x	T_3			S_3			T_2			N_2			C_2			B_2			

d	M_{low}			M_{med}			M_{high}			
	r	m	b	r	m	b	r	m	b	Codes
	0.78	1.29	-0.08	0.38	1.11	-0.03	0.49	0.85	0.05	2D vs. 2D
	0.72	1.03	0.06	0.71	0.66	0.00	0.49	0.65	0.24	3D vs. 3D
	0.72	1.89	-0.23	0.60	1.32	-0.06	0.54	1.39	-0.19	2D vs. 3D
	0.75	1.59	-0.15	0.52	1.20	-0.04	0.52	1.13	-0.06	Any
	0.46	1.08	-0.09	0.65	1.33	-0.32	0.34	1.43	-0.42	2D vs. 2D
	-0.26	-0.46	1.44	0.59	0.55	0.43	0.41	0.20	0.76	3D vs. 3D
	0.40	1.60	-0.60	0.67	1.07	-0.05	0.51	2.11	-1.04	2D vs. 3D
	0.38	1.25	-0.26	0.66	1.14	-0.13	0.43	1.71	-0.67	Any

r = Correlation coefficient
m = Regression slope coefficient
b = Regression y-intercept coefficient

173x155mm (150 x 150 DPI)

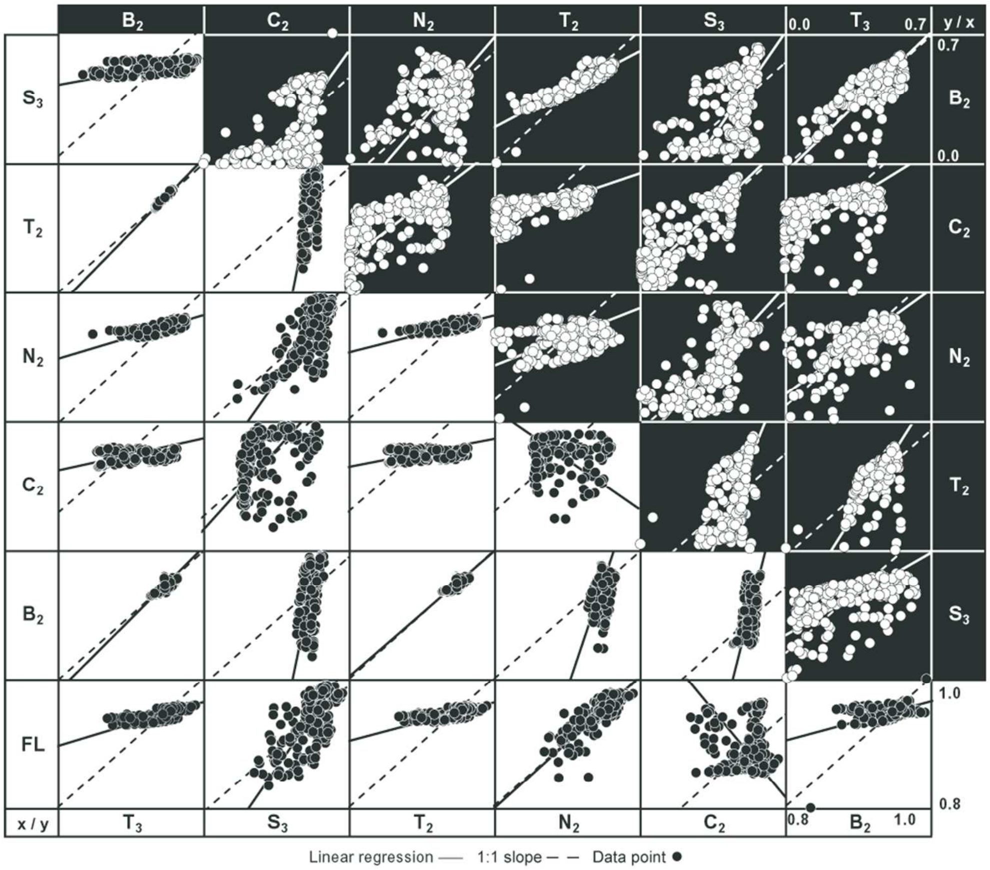

175x154mm (150 x 150 DPI)

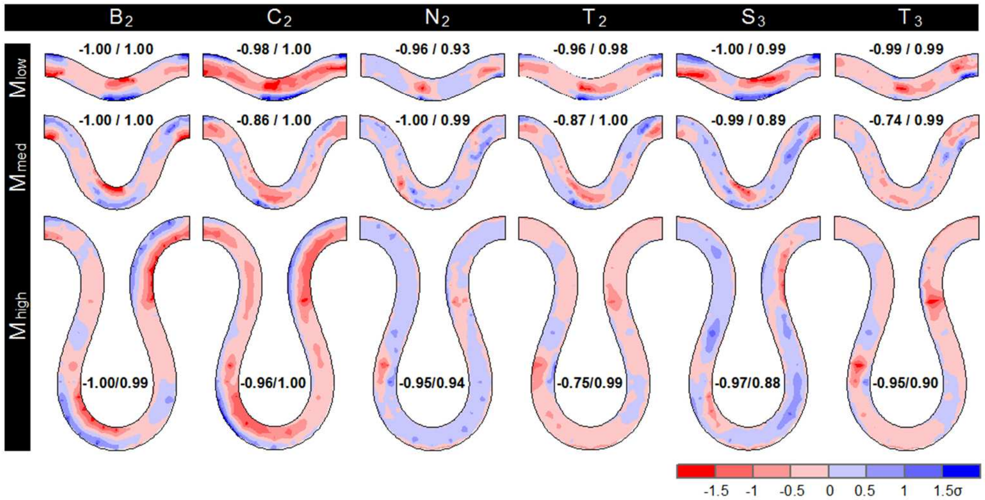

189x97mm (150 x 150 DPI)

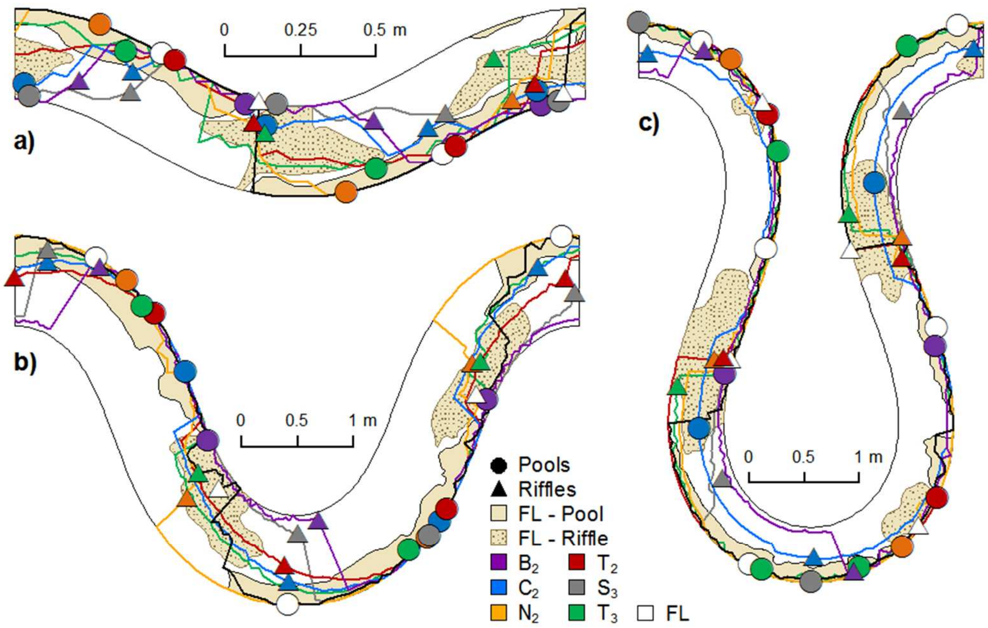

165x110mm (150 x 150 DPI)

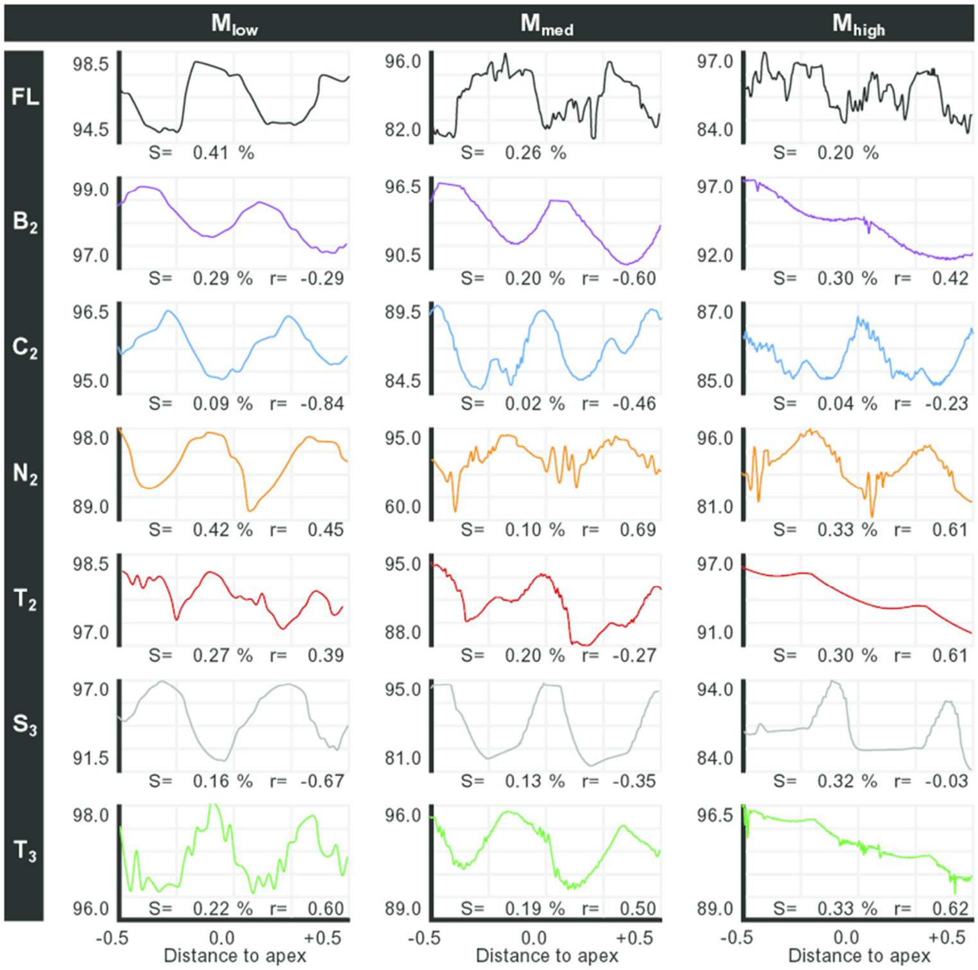

148x145mm (150 x 150 DPI)

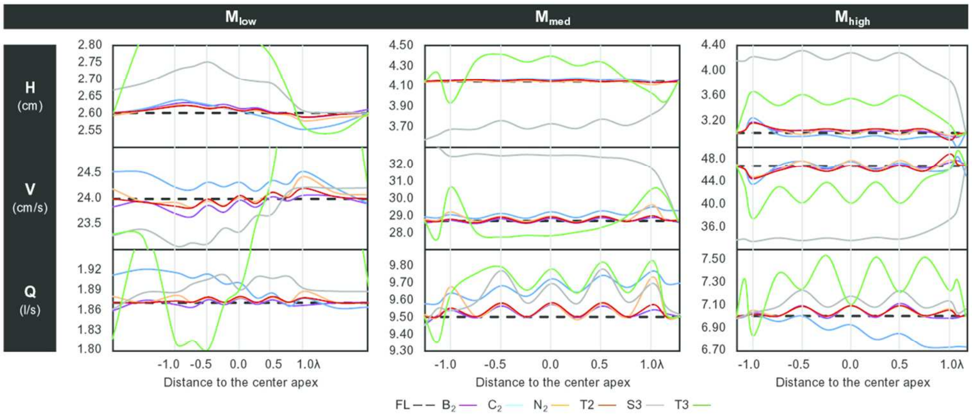

223x97mm (150 x 150 DPI)

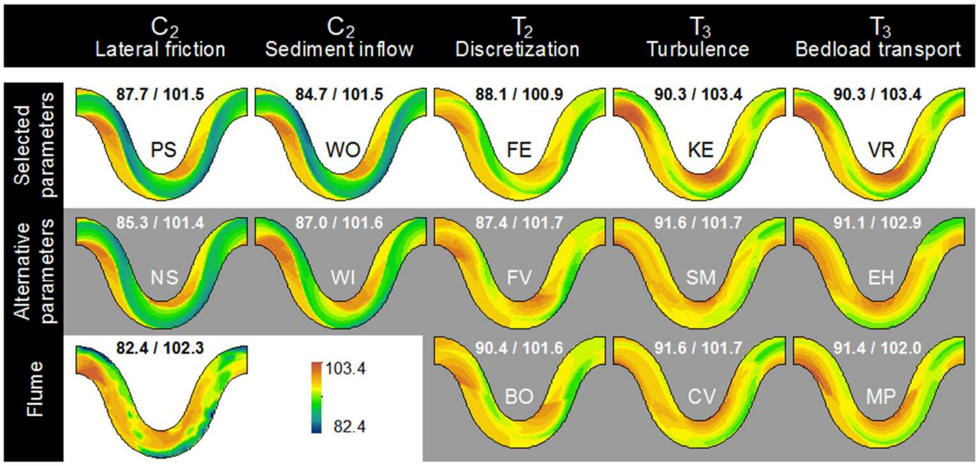

167x82mm (150 x 150 DPI)

a

y / x	PS / WO r	PS / WO m	PS / WO b	NS r	NS m	NS b	WI r	WI m	WI b
FL	0.62	1.20	-0.22	0.68	**1.04**	-0.07	0.78	0.91	0.08
PS / WO				0.86	0.87	0.12	0.87	0.76	0.24
NS							0.94	0.87	0.14

b

y / x	FE r	FE m	FE b	FV r	FV m	FV b	BO r	BO m	BO b
FL	0.64	0.65	0.33	0.69	0.56	0.43	0.60	0.47	0.51
FE				0.91	0.86	0.14	0.92	0.73	0.27
FV							0.89	0.84	0.15

c

y / x	KE / VR r	KE / VR m	KE / VR b	SM r	SM m	SM b	CV r	CV m	CV b	EH r	EH m	EH b	MP r	MP m	MP b
FL	0.76	0.75	0.24	0.65	0.45	0.53	0.80	0.53	0.45	0.75	0.58	0.41	0.74	0.52	0.47
KE / VR				0.71	0.60	0.39	0.83	0.70	0.28	0.78	0.76	0.23	0.92	0.69	0.30
SM							0.92	1.18	-0.17	0.82	1.28	-0.27	0.80	1.15	-0.15
CV										0.89	1.09	-0.08	0.89	0.98	0.02
EH													0.80	0.90	0.10

Lateral friction
NS = No slip
PS = Partial slip

Sediment inflow
WO = Without inflow
WI = With inflow

Spatial discretization
FE = Finite element
FV = Finite volume
BO = Boussinesq (1871, 1872)

Comparison with flume data (FL)

Turbulence closure
KE = k-ε
SM = Smagorinsky (1963)
CV = Constant viscosity

Bedload transport formula
VR = Van Rijn (1984)
EH = Engelund-Hansen (1967)
MP = Meyer-Peter and Müller (1948)

158x94mm (150 x 150 DPI)

a

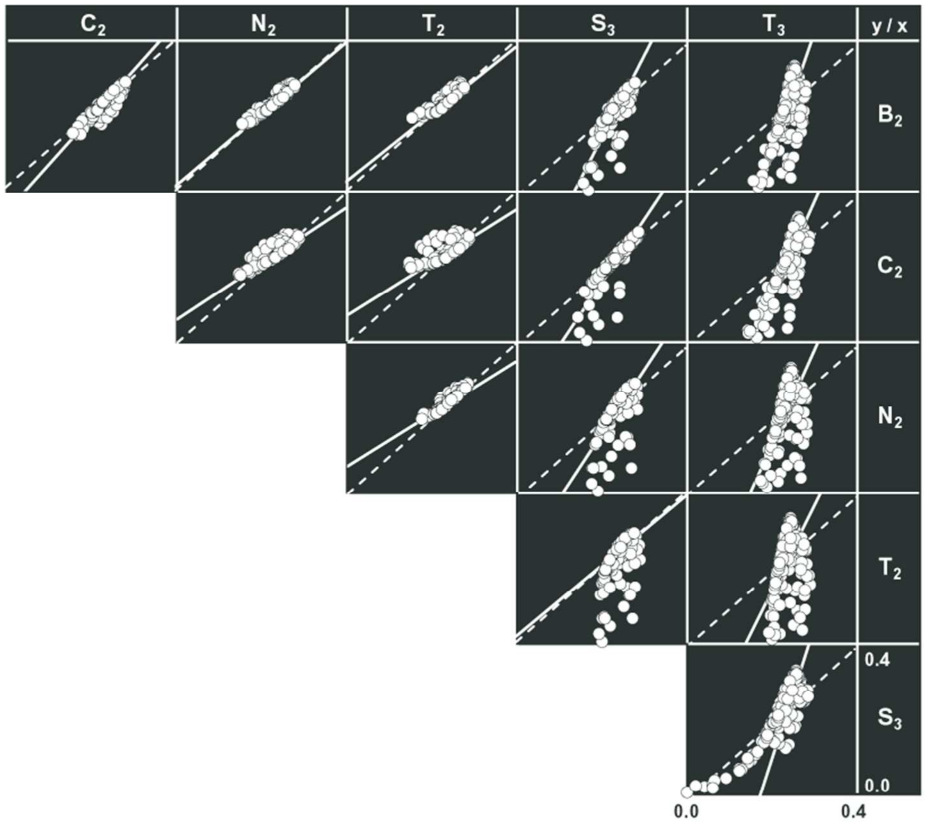

b

y / x	C_2 r	C_2 m	C_2 b	N_2 r	N_2 m	N_2 b	T_2 r	T_2 m	T_2 b	S_3 r	S_3 m	S_3 b	T_3 r	T_3 m	T_3 b
B_2	0.93	1.29	-0.06	0.95	0.96	0.01	0.89	0.89	0.02	0.84	2.18	-0.30	0.70	3.27	-0.56
C_2				0.87	0.74	0.06	0.72	0.70	0.07	0.90	1.69	-0.19	0.84	2.55	-0.40
N_2							0.96	0.94	0.01	0.71	2.28	-0.32	0.53	3.43	-0.60
T_2										0.55	2.43	-0.36	0.35	3.66	-0.65
S_3													0.89	1.50	-0.11

Linear regression —— 1:1 slope – – Data point ●

r = Correlation coefficient; m = Regression slope coefficient; b = Regression y-intercept coefficient

150x164mm (150 x 150 DPI)

a

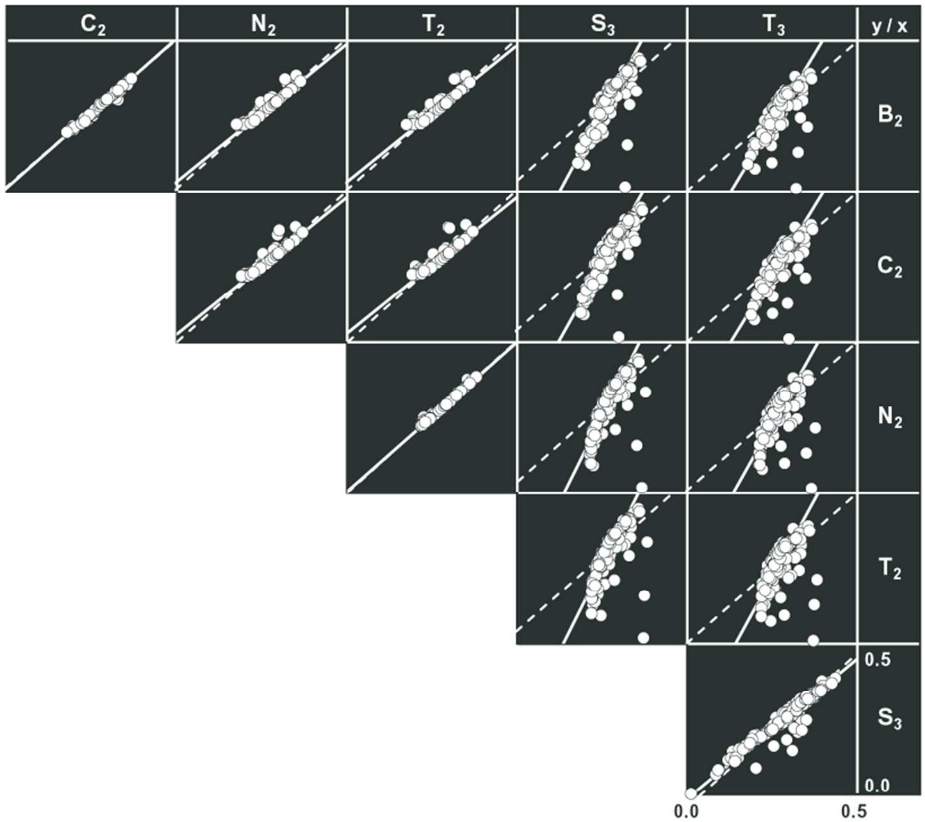

b

C$_2$ r	C$_2$ m	C$_2$ b	N$_2$ r	N$_2$ m	N$_2$ b	T$_2$ r	T$_2$ m	T$_2$ b	S$_3$ r	S$_3$ m	S$_3$ b	T$_3$ r	T$_3$ m	T$_3$ b	y / x
0.99	1.01	0.00	0.97	0.92	0.02	0.95	0.91	0.03	0.83	2.06	-0.26	0.79	1.87	-0.25	B$_2$
			0.96	0.91	0.02	0.94	0.89	0.03	0.86	2.03	-0.26	0.82	1.84	-0.25	C$_2$
						1.00	0.98	0.00	0.72	2.24	-0.31	0.64	2.03	-0.30	N$_2$
									0.68	2.27	-0.32	0.60	2.07	-0.30	T$_2$
												0.96	0.91	-0.01	S$_3$

Linear regression —— 1:1 slope – – Data point ●

r = Correlation coefficient; m = Regression slope coefficient; b = Regression y-intercept coefficient

150x164mm (150 x 150 DPI)

a

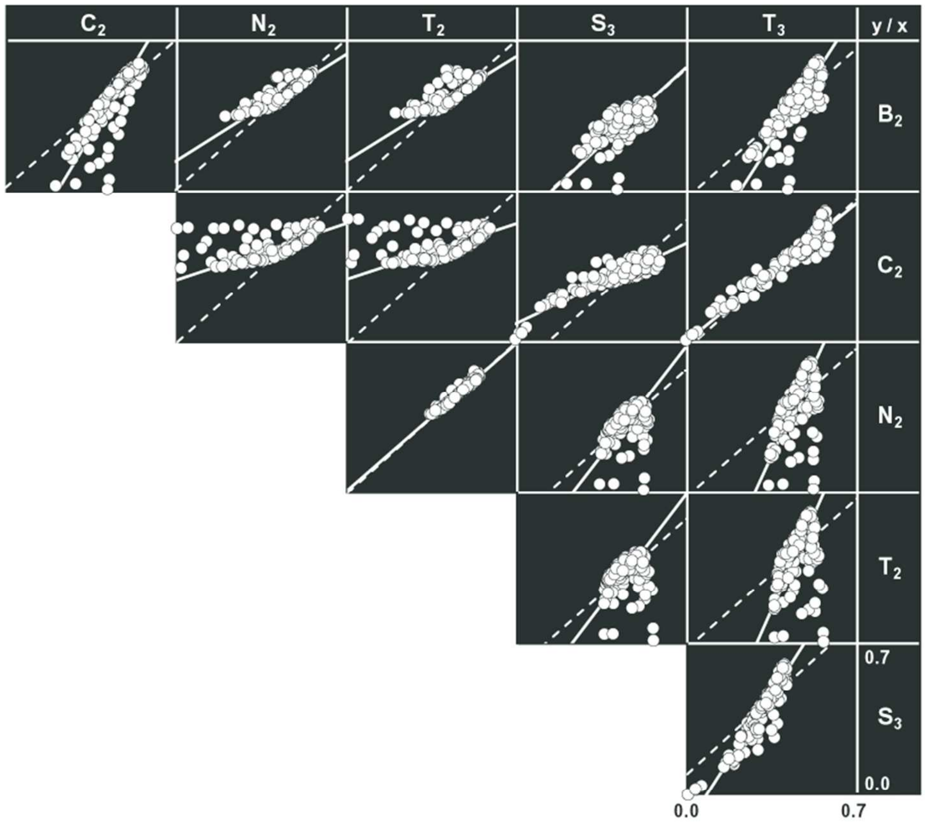

b

y / x	C_2 r	C_2 m	C_2 b	N_2 r	N_2 m	N_2 b	T_2 r	T_2 m	T_2 b	S_3 r	S_3 m	S_3 b	T_3 r	T_3 m	T_3 b
B_2	0.85	1.91	-0.41	0.87	0.71	0.13	0.78	0.69	0.14	0.72	1.03	-0.15	0.82	1.76	-0.39
C_2				0.54	0.37	0.13	0.38	0.36	0.29	0.91	0.54	0.08	0.95	0.92	-0.01
N_2							0.98	0.97	0.01	0.44	1.44	-0.34	0.51	2.47	-0.72
T_2										0.29	1.48	-0.35	0.38	2.54	-0.74
S_3													0.93	1.72	-0.14

Linear regression —— 1:1 slope — — Data point ●

r = Correlation coefficient; m = Regression slope coefficient; b = Regression y-intercept coefficient

150x164mm (150 x 150 DPI)